ChemRxiv™

doi.org/10.26434/chemrxiv.10693025.v1

Two-Dimensional Noble-Metal Dichalcogenides and Phosphochalcogenides

Roman Kempt, Agnieszka Kuc, Thomas Heine

Submitted date: 21/11/2019 • Posted date: 29/11/2019

Licence: CC BY-NC-ND 4.0

Citation information: Kempt, Roman; Kuc, Agnieszka; Heine, Thomas (2019): Two-Dimensional Noble-Metal Dichalcogenides and Phosphochalcogenides. ChemRxiv. Preprint.
https://doi.org/10.26434/chemrxiv.10693025.v1

Noble-metal chalcogenides, dichalcogenides and phosphochalcogenides are an emerging class of two-dimensional materials. Their properties can be broadly tuned via quantum confinement (number of layers) and defect engineering, including metal-to-semiconductor transitions, magnetic ordering, and topological surface states. They possess various polytypes, often of similar formation energy, which can be assessed by selective synthesis approaches. They excel in mechanical, optical and chemical sensing applications, and feature long-term air- and moisture stability. In this review, we summarize the recent progress in the field of noble metal chalcogenides and phosphochalcogenides and highlight the structural complexity and its impact on applications.

File list (2)

ChemArxiv.pdf (1.20 MiB) view on ChemRxiv • download file

Roman_Review_SI.pdf (9.56 MiB) view on ChemRxiv • download file

Two-Dimensional Noble-Metal Dichalcogenides and Phosphochalcogenides

Roman Kempt[a], Agnieszka Kuc[b], Thomas Heine*[a]
[a] Technical University Dresden, Faculty of Chemistry and Food Chemistry, Bergstrasse 66, 01609 Dresden, Germany
[b] Helmholtz-Zentrum Dresden-Rossendorf, Institute of Resource Ecology, Permoserstrasse 15, 04318 Leipzig, Germany

Abstract: Noble-metal chalcogenides, dichalcogenides and phosphochalcogenides are an emerging class of two-dimensional materials. Their properties can be broadly tuned via quantum confinement (number of layers) and defect engineering, including metal-to-semiconductor transitions, magnetic ordering, and topological surface states. They possess various polytypes, often of similar formation energy, which can be assessed by selective synthesis approaches. They excel in mechanical, optical and chemical sensing applications, and feature long-term air- and moisture stability. In this review, we summarize the recent progress in the field of noble metal chalcogenides and phosphochalcogenides and highlight the structural complexity and its impact on applications.

1. Introduction

Noble-Metal chalcogenides (NMCs) are known since the late 19th century,[1] however, their dichalcogenide forms (NMDCs: MX_2, M = Pd, Pt, X = S, Se, Te) have been well-characterized only in the 20th century by the groups of Grønvold[2–6] and Hulliger.[7,8] Many NMDCs, e.g., $PtSe_2$ and $PdTe_2$,[9] and also some of the less well-known noble-metal phosphochalcogenides (NMPCs),[10,11,12] are layered materials. However, the interest in these has been limited due to their high cost, and little research has been carried out after the 1960's, until the "rediscovery" of NMDCs in 2014[13] as potential two-dimensional (2D) material candidates. As for application in 2D devices only one or few layers are required, the economic bottleneck is removed, which boosted research efforts in the field during the past few years.
NMDCs gained a lot of attention as new members of the 2D family due to a layer-controllable metal-to-semiconductor transition,[14,15] where few layers and bulk feature topological properties as Dirac type-II semimetals.[16–19] They showed an outstanding performance as sensors, e.g., for pressure or for specific molecular species.[20–24] Their chemistry, which includes highly anisotropic structural features,[25] low-energy differences between different polymorphs,[26] controllable phase changes,[27–30] and interesting catalytic properties,[15,31–34] is quite different from that of the well-known transition-metal dichalcogenides (TMDCs), such as MoS_2 or WSe_2.[35] This chemistry is affected by strong electron correlation and by relativistic effects, which render their theoretical investigation challenging. To allow for the direct comparison, this review contains a recalculation of the structural, vibronic, and electronic features of these materials on grounds of density-functional theory (DFT, see Methods). This allows for a consistent comparison between theory, as well as between theory and experiment, in particular for phase stabilities and vibrational spectra. With that, we provide an extensive characterization of NMDCs and NMPCs, highlighting recent developments in the field. A complementary, detailed review focused on the application of NMDCs has recently be published by Pi *et al.*,[36] and an in-depth analysis of mechanical and photocatalytic properties NMDC monolayers by Xiong *et al.*[37] Here, we put an emphasis on the phase stabilities and transitions of the NM(D/P)Cs, which define if and how single or few layer materials can be obtained in experiment.

2. Structures of layered NM(D/P)Cs

The palladium and platinum dichalcogenides have been first synthesized and characterized in the early- to mid-1900s.[2–6,38] They feature rich polymorphism corresponding to a complicated phase diagram.[6] Before we turn to recent advances in their synthesis as 2D materials, we discuss their structural prototypes, stabilities, and structural relations.
The platinum dichalcogenides PtX_2 favor the CdI_2-type structure, which is common to Group 4 and referred to as the 1*T*-phase (Fig. 1b).[3,34,39] For group 5 and 6 TMDCs, the stability of the MoS_2 type (called 2*H*-phase, Fig. 1c) is higher, which can be related to the increasing *d*-electron count.[40–42] For TMDCs with larger *d*-electron count, the 2*H*-phase is typically unstable.[41]
For PtS_2, we determine the 2*H*-phase to be instable, whereas for $PtSe_2$, we obtain a large energy difference to the 1*T*-phase of 144 kJ mol^{-1} (all energies are given per formula unit). Nonetheless, 2*H*-$PtSe_2$ has been observed experimentally in few-layer nanosheets by Wang *et al*.[28] Furthermore, Lin et al.[27] show a controllable process to obtain mixed 1*T*-2*H*-$PtSe_2$ structures. This illustrates that these high-energy structures can be accessible in nanoscale processes.
Concerning the palladium dichalcogenides, we predict much smaller energy differences below 57.6 kJ mol^{-1} between the different polymorphs (Tab. 1). In recent publications, these relatively small differences lead to some controversy in the prediction of the most stable phase for fewer layers.[13,26,43,44] In experiment, $PdTe_2$ also prefers the 1*T*-phase[45,46], whereas both PdS_2 and $PdSe_2$ adopt a completely different layered structure with an orthorhombic unit cell, here called 2*O*-phase (Fig. 1a).[2,4,7,47–49] This structure is quite surprising due to its unique pentagonal tiling.[50] While the 2*H* and 1*T* prototypes, as well as their differently stacked (3*R*) and distorted variants (1*T*', T_d, $AuTe_2$)[29,42], are still quite similar to each other, the 2*O* structure seems to be particular.

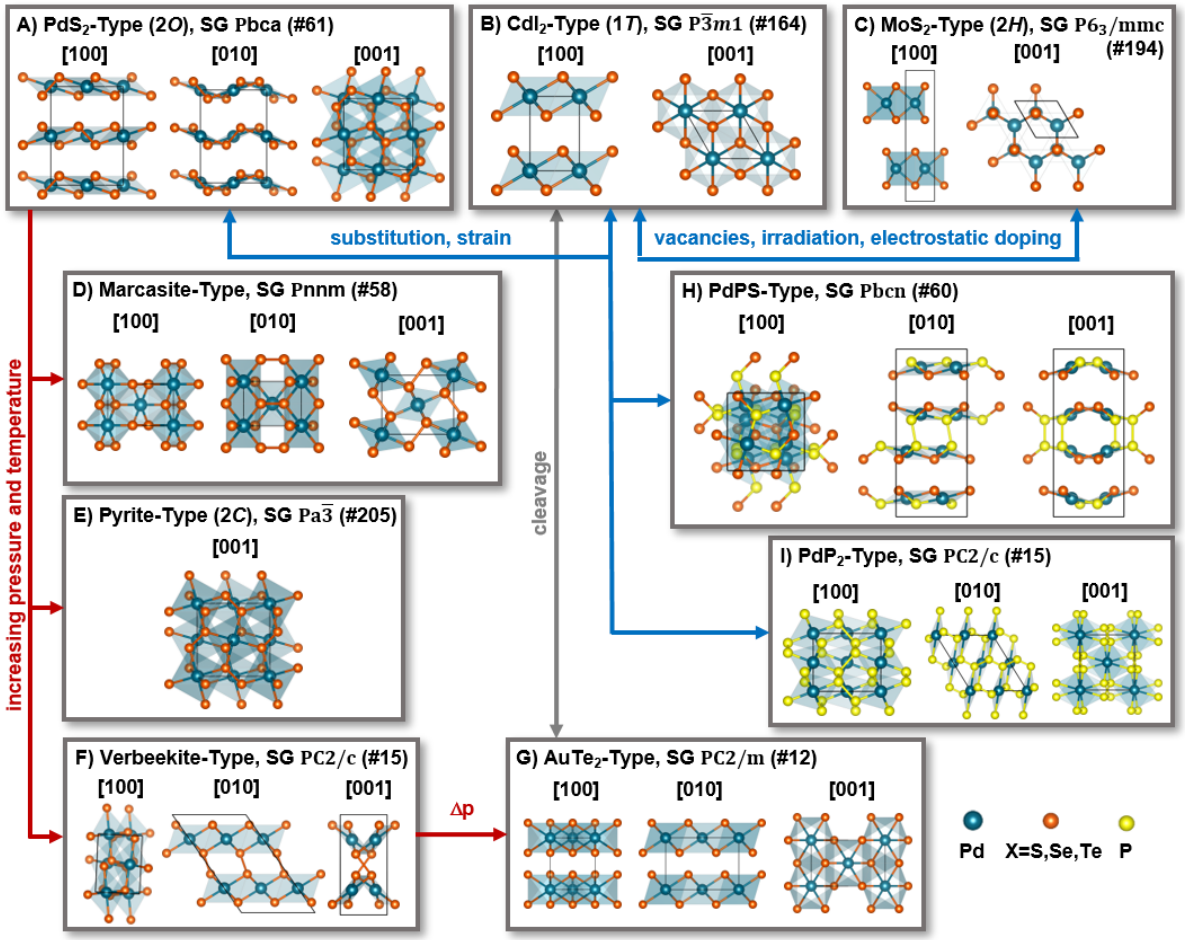


Figure 1 - Overview of the main structural prototypes of the NM(D/P)Cs. Commonly used abbreviations are given in parentheses, as well as the space group SG and the SG number #. Structures are shown along the perspectives indicated in brackets. Possible means to achieve phase transitions are shown with arrows.

To provide insight on the stability and properties of these phases, we show that the structure of PdS_2 and $PdSe_2$ (Fig. 1a) is related to the pyrite-type structure (Fig. 1e).[7] Then, we connect the pyrite structure to its high-pressure phases (marcasite[51] and verbeekite[52] in Fig. 1d and Fig. 1f) and show its transformation back to the 1*T*-phase (Fig. 1b). In the next step, we turn to even more chemically complex systems, involving substitution and defects. We show similarities between the 2*O*-phase and the structure of PdPS (Fig. 1h), which occurs as an intermediate to the PdP_2 structure (Figs. 1i).

2.1. Relation of PdS_2-type and CdI_2-type

Simple concepts, such as the oxidation state and charge distribution, help to identify the key factors for the structural stability of these polymorphs.[40] Within the ionic counting scheme, the metal centers in the octahedrally coordinated 1*T*-phase formally have an oxidation state of +IV.[46] Platinum dichalcogenides with this oxidation state are stable due to the involvement of *f*-orbitals, whereas the palladium dichalcogenides prefer to lower the oxidation state to +II. This can be achieved by pairing the chalcogen atoms to form $(X_2)^{2-}$ dimers, leading to the pyrite- and marcasite-type structures, both with octahedral coordination of the metal centers (Fig. 2 and Fig. 3a). Phase transitions between the 1*T*, marcasite, and pyrite structures have been observed in $IrTe_2$[80] and $CoTe_2$.[53]

We support the validity of these simple chemical descriptors with the Hirshfeld charge analysis (Fig. S1). There, we show a large charge transfer (corresponding to a higher oxidation state) in the 1*T* structures of PdS_2 and $PdSe_2$ compared with a smaller charge transfer (corresponding to a lowered oxidation state) in the pyrite-like phases. In the case of $PdTe_2$, the charge transfer has similar magnitude between the 1*T*- and pyrite-phase, indicating no change in oxidation state. Since Te-Te dimer formation is less likely, $PdTe_2$ prefers the 1*T*-phase.

The ground-state structure of PdS_2 and $PdSe_2$ compared with the pyrite prototype has lower symmetry, which avoids the d^8 electron configuration in the octahedral crystal field. Therefore, one axis is elongated, imposing a change to a square-planar coordination. This leads to a novel structure with AB-stacked, buckled layers, which can be expressed in the sum formula $Pd^{2+}(X_2)^{2-}$. Furthermore, one lattice vector (either *a* or *b*) is slightly elongated to avoid degenerate *d*-states on the metal centers. Consequently, the PdS_2-type structures are generally semiconductors,[7] but close their band gaps under pressure.[48,49,54]

Formula	Structure	Lattice	Band gap	$E_{exfl.}$	Synthesis	Properties and Applications
PdS_2	PdS_2[2]	a = 5.460 b = 5.416 c = 7.531	0.7 eV[7] (indirect)	0.31 J m^{-2}*	chemical vapor transport[48]	superconducting at ~16 GPa[48]
	CdI_2* (+44.4 kJ mol^{-1})	a = b = 3.483* c = 5.226*	metallic*	0.32 J m^{-2}*	-	single-material logical junctions[43]
$PdSe_2$	PdS_2[2]	a = 5.741 b = 5.866 c = 7.691	0.5 eV[109] (indirect)	0.33 J m^{-2}*	self-flux method[50] chemical vapor deposition[25]	high mobility FETs [47] polarization-sensitive Photodetectors[24]
	marcasite[51] (+44.8 kJ mol^{-1})	a = 4.873 b = 6.013 c = 3.930	metallic*		high pressure / high temperature, e.g., in diamond anvil cells	-
	pyrite[51,54] (+38.6 kJ mol^{-1})	a = b =c = 6.100	metallic[49]			superconducting at 23 GPa[49]
	verbeekite[52] (+1.4 kJ mol^{-1})	a = 10.93 b = 4.154 c = 6.710 β = 125 °	0.85 eV* (direct)*			-
	CdI_2* (+31.7 kJ mol^{-1})	a = b = 3.734* c = 4.889*	metallic*	0.40 J m^{-2}*	-	single-material logical junctions[43]
$PdTe_2$	CdI_2[45]	a =b = 4.037 c = 5.126	metallic[7]	0.85 J m^{-2}*	molecular beam epitaxy[66,67]	Dirac Type-II Fermions and superconducting[16,17,19,67]
	pyrite* (+13.6 kJ mol^{-1})	a = b = c = 6.561	metallic*		-	-
PtS_2	CdI_2[3,7]	a = b = 3.543 c = 5.039	0.7 eV[7] (indirect)	0.20 J m^{-2}*	vapor assisted conversion[62]	high-gain phototransistor[81] chemical sensors[62]
$PtSe_2$	CdI_2[3]	a = b = 3.728 c = 5.081	metallic	0.51 J m^{-2}*	epitaxial growth[15] thermally assisted conversion[22]	chemical sensors[20,22] piezoresistive sensors[21]
	MoS_2 (+162 kJ mol^{-1})	a = b = 3.507* c = 11.334*	metallic*	1.35 J m^{-2}*	chemical vapor deposition[28]	-
$PtTe_2$	CdI_2[3]	a = b = 4.026 c = 5.221	metallic[7]	0.28 J m^{-2}*	self-flux method[72]	Dirac Type-II Fermions[17,72]
	MoS_2 (+100 kJ mol^{-1})	a = b = 3.879 c = 11.957	metallic*	0.76 J m^{-2}*	-	-
PdPS	PdPS[12]	a = 13.31 b = 5.678 c = 5.693	0.65 eV [9,119] (indirect*)	0.31 J m^{-2}*	elementary reaction[119]	photocatalytic water splitting[114]
PdPSe	PdPS[9,119]	a = 13.57 b = 5.824 c = 5.856	0.15 eV [9,119] (direct*)	0.33 J m^{-2}*	elementary reaction[119]	photocatalytic water splitting[114]
PtTe	PtTe	a = 6.860 b = 3.960 c = 7.044 β = 109 °	metallic* [61]	0.95 J m^{-2} * [61]	elementary reaction[120]	oxygen reduction reaction[61]

Table 1 - Sum formula, structure prototype, lattice parameters in Angström and degrees, band gap in eV, reported synthesis, selected properties and applications of layered NM(D/P)Cs. Entries marked with an asterisk (*) refer to theoretical predictions from this work or from the given citation.

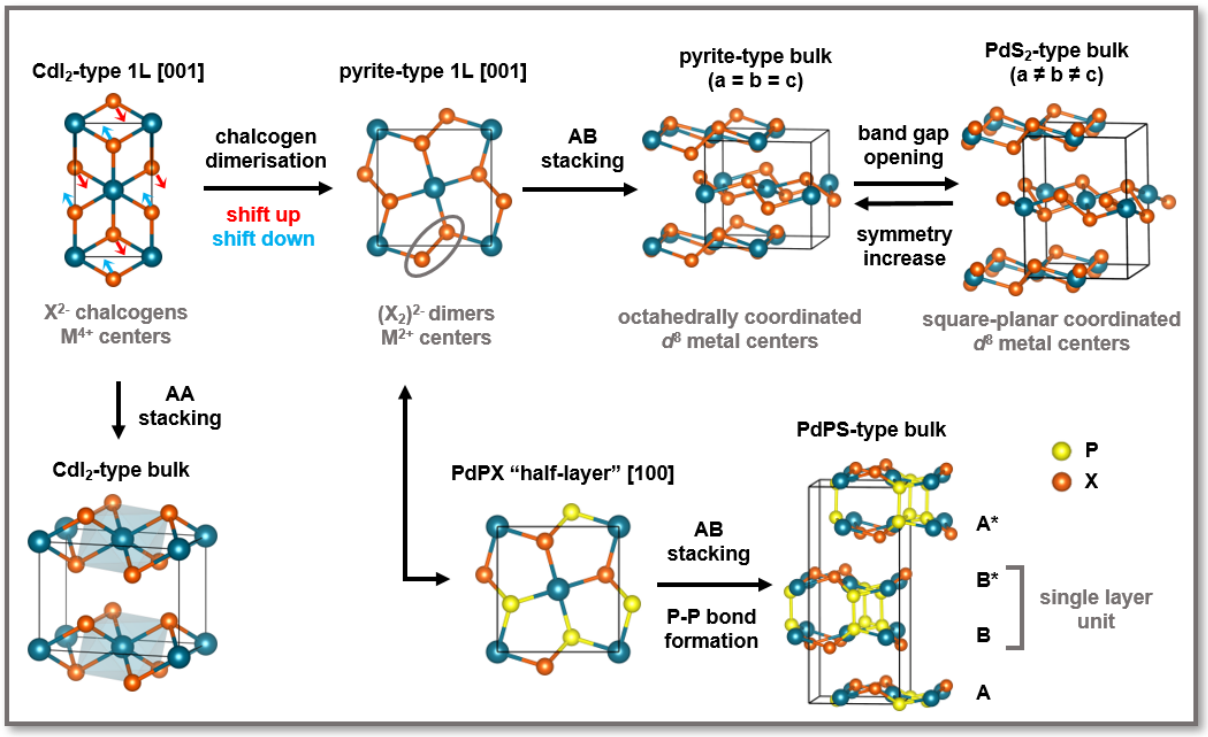


Figure 2 – Structural relations between the PdS_2 and PdPS structures. The CdI_2 prototype can be transformed via the pyrite-type to then PdS_2-type structure, and the pyrite structure is the parent for the PdPS structure. Note that the PdPS structure consists of six atomic layers, two of them are connected by inversion symmetry and phosphorus bonds. Layers that are antisymmetric with respect to each other are indicated with an asterisk (*).

2.2. High-Energy Structures

Under pressure, the PdS_2-type structure reversibly transforms to the pyrite-type structure.[48,49,51,52,54,55] The pyrite-phase competes with the marcasite-type structure, as they are close in energy (ΔE of only 6.2 kJ mol^{-1} for $PdSe_2$). This is well known for these two phases, since they differ mainly in the orientation of the chalcogen dimers (Fig. 3b).[53] Larchev and Popova[51] observed the marcasite-phase of $PdSe_2$ at 7.5 GPa and below 900°C, whereas the pyrite-phase was preferred above this temperature.

Intermediately, other phases with reduced interlayer distance can occur.[55] Concerning PdS_2, much higher pressures of 16 GPa are needed to obtain it in the pyrite-phase.[48] Pyrite-PdS_2 becomes superconducting at a critical temperature of 8 K at 37.4 GPa[48], while pyrite-$PdSe_2$ requires 13.1 K and 23 GPa.[49]

So far, the synthesis of $PdTe_2$ in the pyrite-phase has not been reported. At pressures above 15.7 GPa and room temperature (or 5 GPa at 300°C), Soulard *et al.*[46] observed a continuous phase transition, where the interlayer Te-Te bond distances become shorter than the intralayer Pd-Te bond distances. This indicates that Te-Te dimers could be formed at elevated temperatures and pressures and may lead to pyrite-$PdTe_2$.

To date, there are no reports on the synthesis of PdS_2 or $PdSe_2$ in the 1*T*-phase either. The structural element that decides if whether the 1*T*-phase is more stable than the 2*O*-phase are the chalcogen dimers. The chalcogen states are also the dominating states just below the Fermi level, as confirmed by the atom-projected density of states (Figs. S2-4). Hence, we expect that laser irradiation or electrostatic doping, as shown for few-layer $MoTe_2$,[56] are promising approaches to induce a phase transformation. From the relations of their structural prototypes, we conclude that uniform pressure is unlikely to transform 2*O*-PdS_2/Se_2 to 1*T*-PdS_2/Se_2, because the latter have larger cell volumes.

An indirect approach to obtain 1*T*-$PdSe_2$ via a high-energy-phase has been suggested by Lei *et al.*:[29] At a temperature of 1600 K and a pressure of 11.5 GPa, 2*O*-$PdSe_2$ undergoes a phase transition to the verbeekite structure (Fig 1f and Fig. 3c), as shown by Selb *et al.*[52] Verbeekite-$PdSe_2$ was found as a mineral first[57] and appears to be a stable polymorph of $PdSe_2$ ($\Delta E \approx 1.4$ kJ mol^{-1}), which is closer to the structure of PdP_2 (Fig. 1i).[11,52] Lei *et al.*[29] predict that verbeekite-$PdSe_2$ under pressure may transform to the slightly distorted 1*T* structure known as $AuTe_2$-type (Fig. 3c), and few-layer 1*T*-$PdSe_2$ may then be cleaved from this phase.

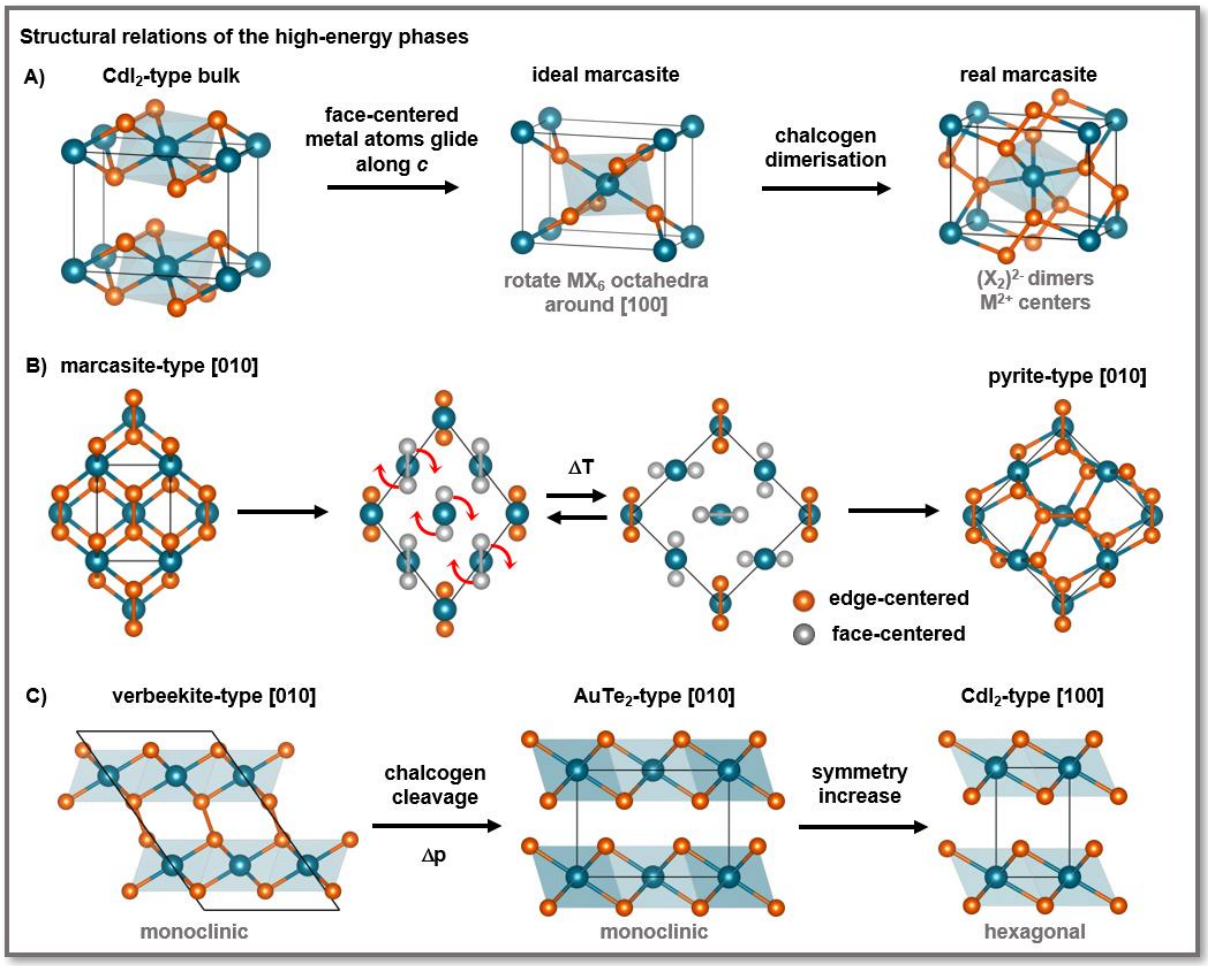


Figure 3 – A) Relation of the 1*T* prototype to the marcasite prototype, B) relation of the marcasite prototype to the pyrite structure, C) relation of the verbeekite and 1*T* structures.

2.3 Ternary Metal Chalcogenides, Phosphides, and Beyond

In addition to pressure and temperature, substitution and defects also lead to unique structural motifs amongst the palladium dichalcogenides. Hulliger[7,9] showed that the ternary mixture PdSSe remains in the PdS_2-type, whereas PdSeTe already occurs in the CdI_2-type. This indicates that there exists a mixture of $PdSe_{1+x}Te_{1-x}$ for $0 < x < 1$, where the 1*T*-phase becomes more stable, because the formation of chalcogen-chalcogen dimers is no longer favorable.

On the other hand, the ternary mixtures PdPS and PdPSe adopt a novel, layered structure, which is an intermediate between the PdP_2 and PdS_2 structures.[9,12] It features the PdS_2-type stacking, but has additional covalent interlayer P-P bonds (Fig. 2).

Lastly, introducing chalcogen vacancies in $PdSe_2$ is interesting for phase transformations and resistive-switching memory devices, because such defects have low diffusion barriers.[58] A lot of selenium vacancies can lead to an 'interlayer fusion', as shown by Lin *et al.*[59] The resulting material has a new layered crystal structure, with the sum formula Pd_2Se_3, which can be an interesting component in heterojunctions.[60] In $PtTe_2$, removing half of the chalcogen atoms to obtain PtTe yields a different layered structure with high basal plane activity towards oxygen reduction reaction and actually metallic monolayers.[61]

3. Synthesis

The first synthetic approaches to obtain bulk NM(D/P)Cs required reactions at high temperatures over the course of several weeks.[2–4,54] The synthesis methods for NM(D/P)C materials have, been strongly improved in the recent years, when these materials regained scientific interest due to their layered bulk forms. Thin layers of these materials can be accessed by alternative synthesis approaches, such as Chemical Vapor Deposition (CVD) or molecular beam epitaxy (MBE).

In 2015, $PtSe_2$ monolayers were successfully grown as high-quality, single-crystalline films by Wang *et al.*[15] The authors showed that a low growth temperature of 270°C was needed to directly selenize a Pt(111) surface. Due to the necessary ultrahigh vacuum and a difficult transferring process, Dong and coworkers[28] proposed an alternative method: CVD based on H_2PtCl_6 and selenium precursors in the temperature range of 300-900°C on a sapphire substrate. This approach results in $PtSe_2$ nanosheets, which are easier to transfer to a poly(methyl-methacrylate) substrate. Both approaches can yield the metastable 2*H*-$PtSe_2$ form.[27]

A more scalable approach was reported by Yim *et al.*,[22] who employed thermally assisted conversion on a Si/SiO_2 substrate. This method is remarkable due to the low growth temperature of 400°C, allowing to obtain polycrystalline $PtSe_2$ films with nanometer-sized grains[21] in a directly compatible fashion with back-end-of-line semiconductor processing.

These approaches are, however, more difficult to apply to PtS_2 due to the competing non-layered PtS phase.[62,63] Monolayer PtS_2 has been obtained via mechanical exfoliation[64], which limits the flake size to small lateral dimensions. Xu *et al.*[62] reported the growth of wafer-scale PtS_2 films, but due to the need to convert the PtS phase to PtS_2 by varying the sulfur vapor pressure during annealing, controlling the surface morphology and thickness is more challenging.[63] The same challenge occurs for PdS_2,[4] which has a different structure and has not been exfoliated yet. Single-crystalline bulk PdS_2 can be obtained via chemical vapor transport.[48]

In 2017, 9 nm thick 2*O* $PdSe_2$ was successfully obtained by Chow *et al.*[47] via a self-flux method at 850°C over the course of 50 h. Oyedele *et al*.[50] used the same synthesis approach and managed to mechanically cleave monolayers from the as-grown material. In both cases, the unique pentagonal Cairo-tiling of this structure was maintained.[50] In 2019, the controllable CVD growth of 2*O*-$PdSe_2$, ranging from 2 to 20 layers on gold foil, has been reported by Jiang *et al.*[25], showing highly anisotropic ribbon formation, due to the orthorhombic crystal structure. Concerning the tellurides, the synthesis of the bulk materials is rather straight-forward,[3,45,65] but few-layer $PtTe_2$ and $PdTe_2$ are difficult to obtain. Li *et al*.[66] used MBE to grow $PdTe_2$ with varying thicknesses down to four layers on a bilayer graphene. Liu *et al*.[67] employed MBE on a $SrTiO_3$(001) surface to obtain $PdTe_2$ between 1 to 20 layers, but more scalable approaches will have to be developed in the future.

In general, all of the layered NMDCs have exfoliation energies that allow for mechanical exfoliation ($E_{exfl.} < 1 J/m^2$, Tab. 1). Some of them, e.g., $PdTe_2$, are clearly much harder to exfoliate than, for example, graphene. We want to highlight the possibility to exfoliate the NMPCs (Tab. 1), which have not been exfoliated to date. If mechanical exfoliation is not possible, bottom-up approaches will have to be developed.

4. Properties and Applications

In this section, we discuss the characterization of NM(D/P)Cs via Raman spectroscopy, their electronic properties depending on the layer thickness, and their applications.

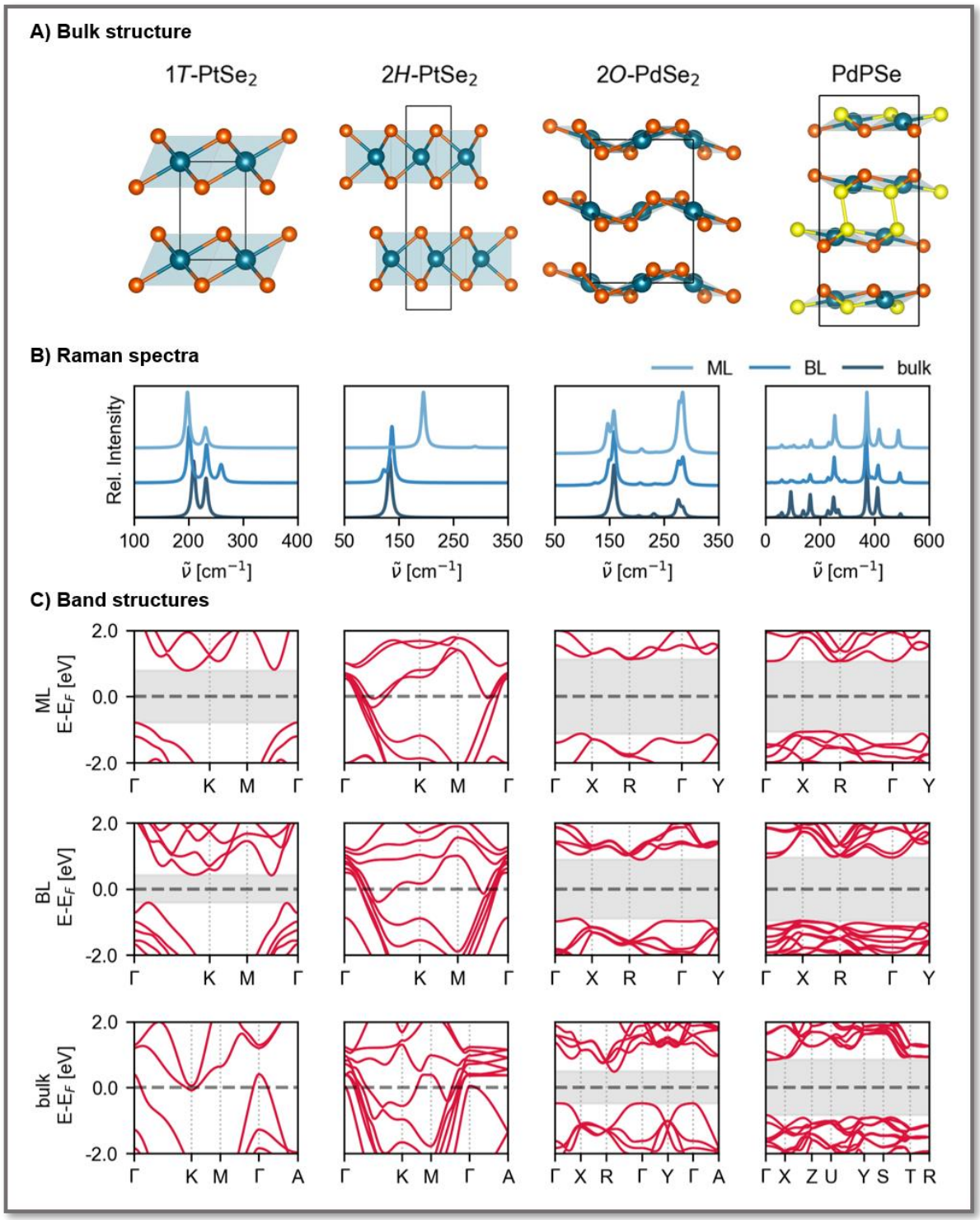


Figure 4 – Calculated Raman spectra and band structures for monolayer (ML), bilayer (BL) and bulk polymorphs of some exemplary layered NM(D/P)Cs.

4.1 Platinum Dichalcogenides

4.1.1. Electronic Properties

The PtX_2 materials excel in optoelectronic applications and feature strongly layer-dependent properties. The bulk materials range from semiconducting for PtS_2 (Δ = 0.7 eV)[7] to metallic for $PtTe_2$.[7] Hulliger reported a band gap measured via the resistivity of $PtSe_2$ of 0.1 eV, while theoretical investigations predicted semimetallic behavior.[13,68] In 2015, Wang *et al*.[15]

confirmed that the bulk material is semimetallic via angle-resolved photoemission spectroscopy (ARPES) measurements. They confirmed the theoretical predictions[13] that the material undergoes a semimetal-to-semiconductor transition when thinning it down to monolayers, which have a band gap of about 1.2 eV. This fascinating effect was supported by Ciarrochi *et al.*[14] and later-on, Shi *et al*.[32] determined this transition to happen already at three layers. These observations agree with our band structure calculations, even though we tend to overestimate the band gaps with the HSE06 functional (Figs. S5-9). Additionally, our calculations show a semimetal-to-semiconductor transition from bilayer to monolayer $PtTe_2$, with a significant impact of spin-orbit coupling (SOC) on the band structure.

Next to the number of layers, the electronic properties of $PtSe_2$ can be tuned over an even broader range through strain and defect engineering. While defect-free $PtSe_2$ as such is diamagnetic, a transition to a half-metallic ferromagnetic state for monolayer $PtSe_2$ at a critical strain of 5% was predicted,[69] which favors the formation of single Pt vacancies and may cause the *p*-type conductance in $PtSe_2$.. These point defects occur intrinsically in ultrathin 1*T*-$PtSe_2$ layers[70] and Avsar *et al*.[71] verify the emergence of magnetism due to vacancies in ultrathin metallic $PtSe_2$ both experimentally and theoretically, in addition to showing that the layer number determines a ferromagnetic or antiferromagnetic ground-state ordering. The possibility of defect-engineering the magnetic properties of $PtSe_2$ renders it very interesting for spintronics.

Lastly, due to the importance of SOC, exotic new electronic states can be realized in this family of materials. Huang *et al*.[17] predicted that the $\mathbf{P}\bar{3}m1$ symmetry enables the existence of stable, strongly tilted type-II Dirac fermions in 1*T*-$PtSe_2$, which have been experimentally verified in 1*T*-$PtTe_2$.[72] These features might be the cause of the anomalous magnetotransport in $PtSe_2$ microflakes[73], but require further investigation in context of the defect- and strain-induced magnetism.

4.1.2 Applications

The tunability of the electronic properties with the number of layers is intriguing for nanoelectronic and sensing applications. Bulk PtS_2 and $PtSe_2$ feature p-type transport with Seebeck coefficients of 500 $\mu V^{-1} K^{-1}$ and 40 $\mu V^{-1} K^{-1}$, respectively.[7] A few-layer PtS_2 field effect transistor (FET) shows mobilities exceeding 62.5 $cm^2 V^{-1} s^{-1}$ [74] and a few-layer $PtSe_2$-FET featured even higher room-temperature mobilities of 210 $cm^2 V^{-1} s^{-1}$.[75]

Yim *et al*.[22] built a chemical gas sensor for NO_2 adsorption with ultrafast response times and sensitivity: After selenizing 0.5 nm Pt via thermally assisted conversion, corresponding to varying thicknesses between 3-5 layers[76], the sensor responded upon 10 s exposure to a 100 sccm flow of NO_2 mixture with N_2 carrier gas, where the original resistance was fully recovered in pure N_2 flow at room temperature. The authors determined response/recovery times of 2.0 to 53.7 s and 7.4 to 38.7 s at 0.1-1.0 ppm of NO_2, with a limit of detection below 100 ppb. The superior gas sensing properties of monolayer $PtSe_2$ have been theoretically verified by Sajjad *et al*.[20], hence, controlling the thickness of the $PtSe_2$ films down to the monolayer limit may improve the performance of the sensor. PtS_2 features even lower detection limits of 0.4 ppb for NO_2, but lower sensitivity and higher response/recovery times.[62]

Based on 4 nm $PtSe_2$ films, Yim *et al*.[22] built $PtSe_2$/n-Si Schottky diodes with a maximum responsivity of 490 mA W^{-1} at a wavelength of 920 nm. The photoresponsivity of $PtSe_2$ in the infrared region allows its usage as absorber with tunable sensitivity.[77] The mid-infrared sensitivity is very promising for optoelectronics and could be enhanced by defect-engineering,[78] and the small band gap of 0.21 eV in a bilayer $PtSe_2$ combined with fast carrier dynamics can be exploited for saturable absorbers to generate ultrafast laser pulses.[79] Zeng *et al*.[80] reported $PtSe_2$/GaAs heterojunction photodetectors with peak sensitivity from 650 to 810 nm, where the on/off response speed of 5.5/6.5 µs is the highest among other group-10 TMDCs. The performance of PtS_2 on Al_2O_3/Si substrates as photodetector is lower (300 A W^{-1} at 830 nm),[74] but PtS_2 on h-BN reaches 1560 A W^{-1} at 500 nm.[81] The striking advantage of PtS_2- and $PtSe_2$-based photodetectors are their much lower response/recovery times, compared for example to MoS2 (4 s / 9 s).[82]

The large response of the electronic properties of $PtSe_2$ to strain can be exploited for optical and mechanical sensors.[83] Du *et al*.[84] show that a compressive strain of 3% can induce a semiconductor-to-semimetal transition in a monolayer $PtSe_2$, which is easier to achieve than in MoS_2 due to the low in-plane stiffness of 64 N m^{-1}.

Few-layer $PtSe_2$ is semimetallic and increases the DOS at the Fermi level under strain, giving rise to a large piezoresistive effect. This allowed Wagner *et al*.[21] to construct highly sensitive pressure sensors based on 4.5 nm thick $PtSe_2$ membranes. The sensitivity of these devices was an order of magnitude higher (5.51×10^{-4} $mbar^{-1}$) than those of other nanomaterial-based devices, including graphene, with a negative gauge factor up to -84.8. Boland *et al*.[85] advanced that approach by growing the $PtSe_2$ layers directly on top of flexible polyimide foils, approach suitable for high-frequency applications. By patterning the $PtSe_2$/polyimide membranes in a three-dimensional kirigami fashion, Okogbue *et al.*[86] built FETs with device stretchability above 2000% and tunable electrical conductance and photoresponsivity.

In terms of catalysis, Chia *et al*.[34] determined that the catalytic activity of platinum dichalcogenides for the hydrogen evolution reaction (HER) increases with the size of the chalcogen atoms. $PtTe_2$ outperforms $PdTe_2$ due to the lower overpotential barrier of 0.54 eV vs. the reversible hydrogen electrode (RHE) and due to being less prone to tellurium stripping.[33] The performance towards HER of the bulk material is reasonable, but can be enhanced by increasing the amount of edge sites[87] or by reducing the bulk thickness. Shi *et al*.[32] indicated atomically thin 1*T*-$PtSe_2$ to be a perfect electrocatalyst, featured with a record high HER efficiency comparable to the traditional Pt catalysts.

4.2 Palladium Ditelluride

4.2.1 Characterization

For the platinum dichalcogenides, Raman spectroscopy has been shown to be a powerful method to monitor the layer thickness.[39] Concerning $PdTe_2$, we predict a sizeable shift of the E_g mode by about 50 cm^{-1} going from bulk to a monolayer

(Fig. S10). Li *et al*.[66] reported the growth of four-layer $PdTe_2$ via molecular beam epitaxy, and measured the Raman spectrum for six layers, showing a shift of the E_g mode to higher wavenumbers by about 7 cm^{-1}, whereas the A_{1g} mode remains unchanged.
Due to the in-plane conductivity of $PdTe_2$, we largely overestimate the intensity of the in-plane E_g mode relative to the out-of-plane A_{1g} mode. The prediction of Raman spectra of metallic systems is challenging and will require further investigations. For comparison with experiments, we indicate the position of the out-of-plane A_{1g} mode in grey (Fig. S10). Our calculated bulk frequencies are in excellent agreement with the experiment of Fei *et al*.,[16] hence, we expect valid predictions for fewer layers. There, the influence of layer-layer coupling may lead to the appearance of new modes, which are lower in symmetry than the E_g and A_{1g} bulk modes. These modes might be used to precisely identify the layer number, such as the bilayer mode at 250 cm^{-1} for 1*T*-$PdTe_2$.

4.2.2 Electronic Properties
$PdTe_2$ behaves closer to PtX_2 than to the other palladium dichalcogenides. Bulk 1*T*-$PdTe_2$ is metallic and diamagnetic[7] and was predicted to undergo a transition to a narrow-gap semiconductor (about 0.14 eV) as monolayer[67], while our calculations suggest a semimetallic state upon including SOC (Fig. S11-12). Usually, weak, temperature-independent paramagnetism ($\mu << \mu_B$) is observed,[88] which might be caused by defects.[71] It features rather strong interlayer interactions, but should still be exfoliable with a cleavage energy of 0.85 J/m² (Tab. 1). Because of these interlayer interactions, it can be considered an intermediate between 2D and 3D materials.[89] This intermediate state can lead to exotic electronic features, such as spin-polarized topological surface states, due to band inversion and complex spin textures.[90]
The physics resulting from the intriguing electronic and phononic structure of $PdTe_2$ is still under debate. It gained a lot of attention being the first material featuring both Dirac fermions and superconductivity,[19,91,92] which is the precondition for the emergence of Majorana fermions.[93] A Majorana is an exotic particle, defined as being a fermion that is its own antiparticle. Majoranas can be realized as quasiparticles in condensed matter physics,[94] and are an important component for the realization of quantum information technology. Experimental realization of Majoranas has been reported only recently.[95]
$PdTe_2$ becomes superconducting at temperatures below 2 K.[7,91,96,97] The symmetry of the states causing the superconductivity is still under debate:[98] while there is agreement that it is conventional superconductivity,[18] it remains unclear whether it is of type-I[97] or type-II.[90] Even though the electronic structure of $PdTe_2$ changes strongly with the number of layers, the superconductive state remains robust even down to two layers,[67] and the superconducting surface states are robust under pressure up to 2.5 GPa.[96]
Evidence of topological surface states in $PdTe_2$ was found by Liu *et al.*[91] via ARPES measurements, but the Dirac point was found at the Γ-point deeply below the Fermi level (~1.75 eV). Noh *et al*.[19] found another Dirac cone much closer to the Fermi level (-0.5 eV) at k=(0, 0, ±0.4) which features strong tilting in the k_z-direction.[16,97] These are type-II Dirac semimetals, (where the *k*-space tilting causes an additional momentum-dependent term in the Hamiltonian, which breaks Lorentz invariance).[72,97,99] Only type-II Dirac semimetals allow for Majorana modes, whereas type-I Dirac semimetals do not.[100] Under pressure of 4.7-6.1 GPa, the Dirac cone can be tuned from type-II to type-I.[101]
Another interesting property of Dirac semimetals is the possibility to break either time reversal symmetry or inversion symmetry, and thus split the doubly degenerate Dirac cone into two separate Weyl nodes.[99,102] These feature spin-polarized Fermi arcs as topological surface states, as well as an anisotropic negative magnetoresistivity.[89,103] Because this intrinsic magnetism could be introduced by defects, $PdTe_2$ is an excellent candidate to study Weyl metals and superconductivity at the same time.

4.3 Palladium Disulfide and Diselenide
4.3.1 Characterization
Their unique structural motif allows to precisely determine the number of layers of crystalline 2*O*-PdS_2 and 2*O*-$PdSe_2$ via Raman spectroscopy, because stacks with an odd number of layers have $P2_1/c$ symmetry (no inversion center), whereas stacks with an even number of layers have $Pca2_1$ symmetry (with inversion center).[104] Hence, the second harmonic generation occurs only in stacks with odd layer number.[104] Furthermore, the Raman intensities are highly polarization-sensitive due to the anisotropic crystal structure.[24,25,104]
For polycrystalline samples, extracting the number of layers from the Raman spectrum is more difficult because the layer-dependent wavenumber shifts are small.[50] We predicted the spectra of monolayer, bilayer and bulk 2*O*-PdX_2 (Fig. 4b, Fig. 5, Figs. S13-16), where our calculated frequencies are in good agreement with the experimentally observed ones.[47,50] In the case of 2*O*-$PdSe_2$, the B_{1g}^1 mode increases its splitting to the A_g^1 mode for decreased number of layers, which can be employed in monitoring the exfoliation progress. We choose to label the modes according to Oyedele *et al*.[50] to facilitate comparison to experiments, where the label does not necessarily reflect the symmetry in case of fewer layers. In the case of 2*O*-$PdSe_2$, our calculations show an increase of the intensity of the A_g^3/B_{1g}^3 signals relative to the B_{1g}^1/A_g^1 signals, in excellent agreement with the experiment.[47,50] On the other hand, we generally seem to underestimate the intensity of the bulk A_g^3/B_{1g}^3 signals, as well as the intermediate A_g^2 and B_{1g}^2 signals.
We complement this section with the Raman and IR spectra of the potential 1*T*-PdS_2 and 1*T*-$PdSe_2$ (Fig. S15 and Fig. S16). However, differentiating them from the 2*O*-phase in experiment could be challenging: We predict the bulk 1*T* E_g mode to appear close to the bulk 2*O* B_{1g}^1/A_g^1 signals and the bulk 1*T* A_{1g} signal to be close to the bulk 2*O* A_g^2 signal. Hence, if the 1*T*-phase occurs only as a minor side phase, it is likely to be overlooked. An indication of the presence of

the 1*T*-phase could be the large intensity of the 1*T* bulk A_{1g} signal, especially for the semiconducting 1*T*-PdS_2. While the A_g^2 and B_{1g}^2 signals in the 2*O* bulk usually have small intensities, a strong signal close to the A_g^2 mode could indicate the 1*T*-phase. Furthermore, for fewer layer numbers, the 1*T*-E_g mode shifts significantly, whereas the 2*O* modes do not.

4.3.2 Electronic Properties

Bulk 2*O*-PdS_2 is a semiconductor with an indirect band gap of ≈0.7 eV.[7] We predict an increase of ≈1 eV when going from bulk to monolayer. Wang *et al*.[26] calculated a band gap of 1.6 eV for the monolayer (HSE06 functional), as well as an anisotropic in-plane stiffness of 58 Nm^{-1} in the x-direction and 82 Nm^{-1} in the y-direction, and large hole mobilities up to 339 $cm^2 V^{-1} s^{-1}$. The band gap can be widely tuned via strain[26], where Lan *et al*.[105] predicted PdS_2 to be thermodynamically stable for strains up to 10 %.

Concerning $PdSe_2$ in the 2*O*-phase, there has been some recent controversy considering the band gap of the bulk material.[50,106,107] Hulliger[7] determined a small band gap of 0.4 eV through resistivity measurements. Several theoretical studies predicted a (semi)metal -to-semiconductor transition for bulk 2*O*-$PdSe_2$ due to the underestimation of the band gap with the PBE functional.[50,106,108] This lead to wrong extrapolations based on optical absorbance spectra yielding a zero band gap for bulk $PdSe_2$.[50,80] Yet, Chow *et al*.[47] clearly proofed 9 nm thick 2*O*-$PdSe_2$ to be a semiconductor by integrating it into a FET and they showed that the band gap can be closed by an external electric field. Zhang *et al*.[109] measured a band gap of 0.5 eV for bulk $PdSe_2$ and 1.37 eV for the monolayer. This is in line with our hybrid functional calculations, where we predict a band gap of 0.96 eV for the bulk which increases to 2.3 eV for the monolayer (Fig. 4c and Figs. S17-18). These calculations overestimate band gap values, but correctly reproduce the shifts observed by Li *et al*.[110], who measured a bilayer band gap of 1.15-1.35 eV. This value depends on the growth substrate due to the proximity screening effect.[111]

While neither 2*O*-PdS_2 nor 2*O*-$PdSe_2$ undergo metal-to-semiconductor transition, this has been predicted for the corresponding 1*T*-phase.[13,43] We calculate a band gap of 0.54 eV to 1.7 eV for 1*T*-PdS_2 for bulk and monolayer, respectively, and a semimetal-to-semiconductor transition in 1*T*-$PdSe_2$ with a monolayer band gap of 0.89 eV (Figs. S17-18). The band gaps are about 0.5 eV larger than the ones calculated with PBE.[13] A metal-to-semiconductor transition could be employed in single-material logical junctions with strongly suppressed Schottky barriers.[43]

4.3.3 Applications

Both 2*O*-PdS_2 and 2*O*-$PdSe_2$ feature desirable properties for thermoelectric applications and transistors: Hulliger[7] measured Seebeck coefficients of 240 and 500 $\mu V^{-1}K^{-1}$ for bulk 2*O*-PdS_2 and 2*O*-$PdSe_2$, respectively. Chow *et al*.[47] obtained a large total mobility of ≈216 $cm^2 V^{-1} s^{-1}$ in 2*O*-$PdSe_2$-based FETs after annealing, with an on/off ratio of 10^3. The performance of these devices could be improved further by reducing the number of layers, where monolayers of 2*O*-$PdSe_2$ have been exfoliated mechanically by Oyedele *et al*.[50] A key advantage of these materials is their air- and moisture-stability even as monolayers.[50] Very recently, monolayer $PdSe_2$ has also been grown via CVD by Jiang *et al*.[25]

The optical properties of $PdSe_2$ render it highly advantageous for sensing applications and photocatalysts.[37] Long *et al*.[23] reported a highly sensitive, air-stable, long-wavelength infrared photodetector based on a MoS_2/$PdSe_2$ heterojunction, which has a high photoresponsivity of 42.1 AW^{-1} at 10.6 µm. The specific detectivity (*D**) of this device is as high as 8.21×10^9 Jones, which is an order of magnitude higher than platinum diselenide (~7×10^8 Jones)[78] and graphene (~8×10^8 Jones).[112]

At shorter wavelengths of 780 nm, Zeng *et al*.[107] obtained a photoresponsivity of 300.2 mA W^{-1} with a $PdSe_2$-based photodetector decorated with black phosphorus quantum dots, which features low rise/fall times of 38 and 44 µs, respectively. Wu *et al*.[24] built a graphene/$PdSe_2$/germanium heterojunction, which features high polarization sensitivity for near-infrared imaging (0.2 to 3.04 µm) with a responsivity of 691 mAW^{-1} and rise/fall times of 6.4/92.5 µs. Walmsley *et al*.[113] built phototransistors with rise/fall time constants of ≈156/163 µs, respectively, which are more than two orders of magnitude faster than other noble metal dichalcogenide based phototransistors.

4.4. Nobel metal phosphochalcogenides

The NMPCs have not yet been studied as 2D materials and with this review, we want to encourage more research into this direction. Similar to the 2*O*-phases[37], the NMPCs can be expected to be interesting for photocatalytic applications. Jing *et al*.[114] predict few-layer PdPX to absorb in the visible range and to have matching band edges for the water splitting reaction, which is confirmed by Jiao et al., [115] including the layered $Pd_3(PS_4)_2$.[116] Because a single layer of PdPX consists of two sheets similar to the 2*O* structure, which are connected by inversion symmetry and P-P bonds, their band structures are more complicated (Fig. 4c, Figs. S19-20). The direct and indirect band gap transitions lie very close in energy, where bulk PdPS is an indirect semiconductor and bulk PdPSe is a direct semiconductor. Due to the higher structural complexity, they feature many more visible Raman modes (Fig. 4b and Fig. S21 and Tab. S1).

Methods

Structural properties (Tabs. S2-6) were calculated using Density-Functional Theory as implemented in the Crystal17 software package.[117] Large *k*-grids (above 18x18x18) were selected for optimization and prediction of vibrational spectra employing hybrid functionals. Electronic properties were calculated using AIMS software package[118] with hybrid functionals on tight tier 2 numerical atom-centered orbitals including spin-orbit coupling. For details we refer to the SI.

Acknowledgements

We acknowledge Dr. Augusto Faria Oliveira and Dr. Thomas Brumme for fruitful discussions and technical support. We thank Dr. Lorenzo Maschio and Dr. Carsten Baldauf for supporting us with calculations using Crystal17 and AIMS. We thank the Center for Information Services and High-Performance Computing (ZIH) at TU Dresden for generous allocations of computer time and the project DFG HE 3543/35-1 for financial support.

Keywords: noble-metal dichalcogenides • two-dimensional materials • sensors • density-functional theory • Raman spectroscopy

[1] C. Roessler, *Z. Anorg. Chem.* **1897**, *15*, 405.
[2] F. Grønvold, E. Røst, *Acta Crystallographica* **1957**, *10*, 329.
[3] F. Grønvold, H. Haraldsen, A. Kjekshus, R. Söderquist, *Acta Chemica Scandinavica* **1960**, *14*, 1879.
[4] F. Grønvold, E. Røst, B. Aurivillius, N. A. Eliasson, B. Thorell, *Acta Chemica Scandinavica* **1956**, *10*, 1620.
[5] A. Kjekshus, F. Grønvold, *Acta Chemica Scandinavica* **1959**, *13*, 1767.
[6] T. Olsen, E. Røst, F. Grønvold, A. F. Andresen, E. Hoyer, V. P. Spiridonov, T. G. Strand, *Acta Chemica Scandinavica* **1979**, *33a*, 251.
[7] F. Hulliger, *JOURNAL OF PHYSICS AND CHEMISTRY OF SOLIDS* **1965**, *26*, 639.
[8] F. Hulliger, J. Müller, *Physics Letters* **1963**, *5*, 226.
[9] F. Hulliger, *Structural Chemistry of Layer-Type Phases*, Springer Netherlands, **1976**.
[10] a) S. Rundqvist, *NATURE* **1960**, *185*, 31; b) "Palladium and platinum phosphochalcogenides—Synthesis and properties", can be found under https://www.sciencedirect.com/science/article/pii/0022459671900430.
[11] W. H. Zachariasen, *Acta Crystallographica* **1963**, *16*, 1253.
[12] W. Jeitschko, *Acta Crystallographica Section B: Structural Crystallography and Crystal Chemistry* **1974**, *30*, 2565.
[13] P. Miró, M. Ghorbani-Asl, T. Heine, *Angewandte Chemie International Edition* **2014**, *53*, 3015.
[14] A. Ciarrocchi, A. Avsar, D. Ovchinnikov, A. Kis, *Nature Communications* **2018**, *9*, 919.
[15] Y. Wang, L. Li, W. Yao, S. Song, J. T. Sun, J. Pan, X. Ren, C. Li, E. Okunishi, Y.-Q. Wang et al., *NANO LETTERS* **2015**, *15*, 4013.
[16] F. Fei, X. Bo, R. Wang, B. Wu, J. Jiang, D. Fu, M. Gao, H. Zheng, Y. Chen, X. Wang et al., *PHYSICAL REVIEW B* **2017**, *96*, 41201.
[17] H. Huang, S. Zhou, W. Duan, *PHYSICAL REVIEW B* **2016**, *94*, 121117.
[18] S. Das, Amit, A. Sirohi, L. Yadav, S. Gayen, Y. Singh, G. Sheet, *PHYSICAL REVIEW B* **2018**, *97*, 14523.
[19] H.-J. Noh, J. Jeong, E.-J. Cho, K. Kim, B. I. Min, B.-G. Park, *Physical Review Letters* **2017**, *119*, 16401.
[20] M. Sajjad, E. Montes, N. Singh, U. Schwingenschlögl, *Advanced Materials Interfaces* **2017**, *4*, 1600911.
[21] S. Wagner, C. Yim, N. McEvoy, S. Kataria, V. Yokaribas, A. Kuc, S. Pindl, C.-P. Fritzen, T. Heine, G. S. Duesberg et al., *NANO LETTERS* **2018**, *18*, 3738.
[22] C. Yim, K. Lee, N. McEvoy, M. O'Brien, S. Riazimehr, N. C. Berner, C. P. Cullen, J. Kotakoski, J. C. Meyer, M. C. Lemme et al., *ACS NANO* **2016**, *10*, 9550.
[23] M. Long, Y. Wang, P. Wang, X. Zhou, H. Xia, C. Luo, S. Huang, G. Zhang, H. Yan, Z. Fan et al., *ACS NANO* **2019**, *13*, 2511.
[24] Di Wu, J. Guo, J. Du, C. Xia, L. Zeng, Y. Tian, Z. Shi, Y. Tian, X. J. Li, Y. H. Tsang et al., *ACS NANO* **2019**.
[25] S. Jiang, C. Xie, Y. Gu, Q. Zhang, X. Wu, Y. Sun, W. Li, Y. Shi, L. Zhao, S. Pan et al., *Small* **2019**, *0*, 1902789.
[26] Y. Wang, Y. Li, Z. Chen, *Journal of Materials Chemistry C* **2015**, *3*, 9603.
[27] X. Lin, J. C. Lu, Y. Shao, Y. Y. Zhang, X. Wu, J. B. Pan, L. Gao, S. Y. Zhu, K. Qian, Y. F. Zhang et al., *Nature Materials* **2017**, *16*, 717 EP -.
[28] Z. Wang, Q. Li, F. Besenbacher, M. Dong, *Advanced Materials* **2016**, *28*, 10224.
[29] W. Lei, S. Zhang, G. Heymann, X. Tang, J. Wen, X. Zheng, G. Hu, X. Ming, *Journal of Materials Chemistry C* **2019**, *7*, 2096.
[30] G. H. Ryu, T. Zhu, J. Chen, S. Sinha, V. Shautsova, J. C. Grossman, J. H. Warner, *Advanced materials (Deerfield Beach, Fla.)* **2019**, e1904251.
[31] C. Long, Y. Liang, H. Jin, B. Huang, Y. Dai, *ACS Applied Energy Materials* **2019**, *2*, 513.
[32] J. Shi, Y. Huan, M. Hong, R. Xu, P. Yang, Z. Zhang, X. Zou, Y. Zhang, *ACS NANO* **2019**.
[33] X. Chia, Z.\v. e. Sofer, J. Luxa, M. Pumera, *ACS Applied Materials & Interfaces* **2017**, *9*, 25587.
[34] X. Chia, A. Adriano, P. Lazar, Z.\v. e. Sofer, J. Luxa, M. Pumera, *Advanced Functional Materials* **2016**, *26*, 4306.
[35] a) Yang, Sandoval, Divigalpitiya, Irwin, Frindt, *Physical review. B, Condensed matter* **1991**, *43*, 12053; b) Q. H. Wang, K. Kalantar-Zadeh, A. Kis, J. N. Coleman, M. S. Strano, *Nat. Nanotechnol.* **2012**, *7*, 699; c) P. Joensen, R. F. Frindt, S.R. Morrison, *Materials Research Bulletin* **1986**, *21*, 457.
[36] L. Pi, L. Li, K. Liu, Q. Zhang, H. Li, T. Zhai, *Adv. Funct. Mater.* **2019**, *0*, 1904932.
[37] W. Xiong, K. Huang, S. Yuan, *Journal of Materials Chemistry C* **2019**.
[38] L. Thomassen, *Zeitfschrift für Physikalische Chemie, B2* **1929**.
[39] M. O'Brien, N. McEvoy, C. Motta, J.-Y. Zheng, N. C. Berner, J. Kotakoski, K. Elibol, T. J. Pennycook, J. C. Meyer, C. Yim et al., *2D Materials* **2016**, *3*, 21004.
[40] D. Pasquier, O. V. Yazyev, *2D Materials* **2019**, *6*, 25015.
[41] M. Kertesz, R. Hoffmann, *JOURNAL OF THE AMERICAN CHEMICAL SOCIETY* **1984**, *106*, 3453.
[42] H. Yang, S. W. Kim, M. Chhowalla, Y. H. Lee, *Nature Physics* **2017**, *13*, 931 EP -.
[43] M. Ghorbani-Asl, A. Kuc, P. Miró, T. Heine, *Advanced Materials* **2016**, *28*, 853.

[44] X. Liu, H. Zhou, B. Yang, Y. Qu, M. Zhao, *Scientific Reports* **2017**, *7*, 39995.
[45] M. A. Pell, Y. V. Mironov, J. A. Ibers, *Acta Crystallographica Section C: Crystal Structure Communications* **1996**, *52*, 1331.
[46] C. Soulard, P. E. Petit, P. Deniard, M. Evain, S. Jobic, M.-H. Whangbo, A.-C. Dhaussy, *JOURNAL OF SOLID STATE CHEMISTRY* **2005**, *178*, 2008.
[47] W. L. Chow, P. Yu, F. Liu, J. Hong, X. Wang, Q. Zeng, C.-H. Hsu, C. Zhu, J. Zhou, X. Wang et al., *Advanced Materials* **2017**, *29*, 1602969.
[48] M. A. ElGhazali, P. G. Naumov, Q. Mu, V. Süß, A. O. Baskakov, C. Felser, S. A. Medvedev, *PHYSICAL REVIEW B* **2019**, *100*, 14507.
[49] M. A. ElGhazali, P. G. Naumov, H. Mirhosseini, V. Süß, L. Müchler, W. Schnelle, C. Felser, S. A. Medvedev, *PHYSICAL REVIEW B* **2017**, *96*, 60509.
[50] A. D. Oyedele, S. Yang, L. Liang, A. A. Puretzky, K. Wang, J. Zhang, P. Yu, P. R. Pudasaini, A. W. Ghosh, Z. Liu et al., *JOURNAL OF THE AMERICAN CHEMICAL SOCIETY* **2017**, *139*, 14090.
[51] V. N. Larchev, S. V. Popova, *Inorganic Materials* **1978**, *14*, 611.
[52] E. Selb, M. Tribus, G. Heymann, *Inorganic Chemistry* **2017**, *56*, 5885.
[53] J. A. Wilson, A. D. Yoffe, *Advances in Physics* **1969**, *18*, 193.
[54] C. Soulard, X. Rocquefelte, P.-E. Petit, M. Evain, S. Jobic, J.-P. Itié, P. Munsch, H.-J. Koo, M.-H. Whangbo, *Inorganic Chemistry* **2004**, *43*, 1943.
[55] E. Selb, T. Götsch, O. Janka, S. Penner, G. Heymann, *Zeitschrift für anorganische und allgemeine Chemie* **2017**, *643*, 1415.
[56] a) Y. Wang, J. Xiao, H. Zhu, Y. Li, Y. Alsaid, K. Y. Fong, Y. Zhou, S. Wang, W. Shi, Y. Wang et al., *NATURE* **2017**, *550*, 487 EP -; b) Y. Tan, F. Luo, M. Zhu, X. Xu, Y. Ye, B. Li, G. Wang, W. Luo, X. Zheng, N. Wu et al., *NANOSCALE* **2018**, *10*, 19964.
[57] A. C. Roberts, W. H. Paar, M. A. Cooper, D. Topa, A. J. Criddle, J. Jedwab, *Mineralogical Magazine* **2002**, *66*, 173.
[58] G. D. Nguyen, L. Liang, Q. Zou, M. Fu, A. D. Oyedele, B. G. Sumpter, Z. Liu, Z. Gai, K. Xiao, A.-P. Li, *Physical Review Letters* **2018**, *121*, 86101.
[59] J. Lin, S. Zuluaga, P. Yu, Z. Liu, S. T. Pantelides, K. Suenaga, *Physical Review Letters* **2017**, *119*, 16101.
[60] a) S. Zuluaga, J. Lin, K. Suenaga, S. T. Pantelides, *2D Materials* **2018**, *5*, 35025; b) X. Zhu, F. Li, Y. Wang, M. Qiao, Y. Li, *Journal of Materials Chemistry C* **2018**, *6*, 4494; c) S. S. Naghavi, J. He, Y. Xia, C. Wolverton, *Chemistry of Materials* **2018**, *30*, 5639; d) J. Chen, G. H. Ryu, S. Sinha, J. H. Warner, *ACS NANO* **2019**.
[61] Y. Wang, Y. Li, T. Heine, *JOURNAL OF THE AMERICAN CHEMICAL SOCIETY* **2018**, *140*, 12732.
[62] H. Xu, H.-P. Huang, H. Fei, J. Feng, H.-R. Fuh, J. Cho, M. Choi, Y. Chen, L. Zhang, D. Chen et al., *ACS Applied Materials & Interfaces* **2019**.
[63] D. Zhao, S. Xie, Y. Wang, H. Zhu, L. Chen, Q. Sun, D. W. Zhang, *AIP Advances* **2019**, *9*, 25225.
[64] Y. Zhao, J. Qiao, P. Yu, Z. Hu, Z. Lin, S. P. Lau, Z. Liu, W. Ji, Y. Chai, *Advanced Materials* **2016**, *28*, 2399.
[65] T. R. Finlayson, W. Reichardt, H. G. Smith, *PHYSICAL REVIEW B* **1986**, *33*, 2473.
[66] E. Li, R.-Z. Zhang, H. Li, C. Liu, G. Li, J.-O. Wang, T. Qian, H. Ding, Y.-Y. Zhang, S.-X. Du et al., *Chinese Physics B* **2018**, *27*, 86804.
[67] C. Liu, C.-S. Lian, M.-H. Liao, Y. Wang, Y. Zhong, C. Ding, W. Li, C.-L. Song, K. He, X.-C. Ma et al., *Physical Review Materials* **2018**, *2*, 94001.
[68] a) D. Dai, H.-J. Koo, M.-H. Whangbo, C. Soulard, X. Rocquefelte, S. Jobic, *JOURNAL OF SOLID STATE CHEMISTRY* **2003**, *173*, 114; b) G. Y. Guo, W. Y. Liang, *Journal of Physics C: Solid State Physics* **1986**, *19*, 995.
[69] M. Zulfiqar, Y. Zhao, G. Li, S. Nazir, J. Ni, *JOURNAL OF PHYSICAL CHEMISTRY C* **2016**, *120*, 25030.
[70] H. Zheng, Y. Choi, F. Baniasadi, D. Hu, L. Jiao, K. Park, C. Tao, *arXiv:1808.04719 [cond-mat]* **2018**.
[71] A. Avsar, A. Ciarrocchi, M. Pizzochero, D. Unuchek, O. V. Yazyev, A. Kis, *Nature Nanotechnology* **2019**, 1.
[72] M. Yan, H. Huang, K. Zhang, E. Wang, W. Yao, K. Deng, G. Wan, H. Zhang, M. Arita, H. Yang et al., *Nature Communications* **2017**, *8*, 257.
[73] Z. Li, J. Zhang, Y. Zeng, L. Meng, M. Zhou, W. Wu, *JOURNAL OF PHYSICS-CONDENSED MATTER* **2017**, *29*, 23LT01.
[74] Z. Wang, P. Wang, F. Wang, J. Ye, T. He, F. Wu, M. Peng, P. Wu, Y. Chen, F. Zhong et al., *Adv. Funct. Mater.* **2019**, *6*, 1907945.
[75] Y. Zhao, J. Qiao, Z. Yu, P. Yu, K. Xu, S. P. Lau, W. Zhou, Z. Liu, X. Wang, W. Ji et al., *Advanced Materials* **2017**, *29*, 1604230.
[76] L. Wang, S. Zhang, N. McEvoy, Y.-y. Sun, J. Huang, Y. Xie, N. Dong, X. Zhang, I. M. Kislyakov, J.-M. Nunzi et al., *Laser & Photonics Reviews* **2019**, *13*, 1900052.
[77] C. Yim, N. McEvoy, S. Riazimehr, D. S. Schneider, F. Gity, S. Monaghan, P. K. Hurley, M. C. Lemme, G. S. Duesberg, *NANO LETTERS* **2018**, *18*, 1794.
[78] X. Yu, P. Yu, Di Wu, B. Singh, Q. Zeng, H. Lin, W. Zhou, J. Lin, K. Suenaga, Z. Liu et al., *Nature Communications* **2018**, *9*, 1545.
[79] a) B. Yan, B. Zhang, H. Nie, G. Li, J. Liu, B. Shi, K. Yang, J. He, *Optics Express* **2018**, *26*, 31657; b) G. Wang, K. Wang, N. McEvoy, Z. Bai, C. P. Cullen, C. N. Murphy, J. B. McManus, J. J. Magan, C. M. Smith, G. S. Duesberg et al., *Small* **2019**, *0*, 1902728.
[80] L.-H. Zeng, S.-H. Lin, Z.-J. Li, Z.-X. Zhang, T.-F. Zhang, C. Xie, C.-H. Mak, Y. Chai, S. P. Lau, L.-B. Luo et al., *Advanced Functional Materials* **2018**, *28*, 1705970.
[81] L. Li, W. Wang, Y. Chai, H. Li, M. Tian, T. Zhai, *Advanced Functional Materials* **2017**, *27*, 1701011.
[82] M. Long, P. Wang, H. Fang, W. Hu, *Adv. Funct. Mater.* **2019**, *29*, 1803807.
[83] S. Deng, L. Li, Y. Zhang, *ACS Applied Nano Materials* **2018**, *1*, 1932.
[84] J. Du, P. Song, L. Fang, T. Wang, Z. Wei, J. Li, C. Xia, *Applied Surface Science* **2018**, *435*, 476.
[85] C. S. Boland, C. Ó. Coileáin, S. Wagner, J. B. McManus, C. P. Cullen, M. C. Lemme, G. S. Duesberg, N. McEvoy, *arXiv:1903.11894 [cond-mat, physics:physics]* **2019**.
[86] E. Okogbue, S. S. Han, T.-J. Ko, H.-S. Chung, J. Ma, M. S. Shawkat, J. H. Kim, J. H. Kim, E. Ji, K. H. Oh et al., *NANO LETTERS* **2019**.
[87] S. Lin, Y. Liu, Z. Hu, W. Lu, C. H. Mak, L. Zeng, J. Zhao, Y. Li, F. Yan, Y. H. Tsang et al., *Nano Energy* **2017**, *42*, 26.
[88] A. Kjekshus, W. B. Pearson, *Canadian Journal of Physics* **1965**, *43*, 438.
[89] B.-J. Yang, N. Nagaosa, *Nature Communications* **2014**, *5*, 4898.
[90] O. J. Clark, M. J. Neat, K. Okawa, L. Bawden, I. Marković, F. Mazzola, J. Feng, V. Sunko, J. M. Riley, W. Meevasana et al., *Physical Review Letters* **2018**, *120*, 156401.
[91] Y. Liu, J.-Z. Zhao, L. Yu, C.-T. Lin, A.-J. Liang, C. Hu, Y. Ding, Y. Xu, S.-L. He, L. Zhao et al., *Chinese Physics Letters* **2015**, *32*, 67303.

[92] Y. Wang, J. Zhang, W. Zhu, Y. Zou, C. Xi, L. Ma, T. Han, J. Yang, J. Wang, J. Xu et al., *Scientific Reports* **2016**, *6*, 31554.
[93] A. P. Schnyder, S. Ryu, A. Furusaki, A. W. W. Ludwig, *Phys. Rev. B* **2008**, *78*, 75.
[94] C.W.J. Beenakker, *Annu. Rev. Condens. Matter Phys.* **2013**, *4*, 113.
[95] a) V. Mourik, K. Zuo, S. M. Frolov, S. R. Plissard, E. P. A. M. Bakkers, L. P. Kouwenhoven, *Science (New York, N.Y.)* **2012**, *336*, 1003; b) S. Nadj-Perge, I. K. Drozdov, J. Li, H. Chen, S. Jeon, J. Seo, A. H. MacDonald, B. A. Bernevig, A. Yazdani, *Science (New York, N.Y.)* **2014**, *346*, 602.
[96] H. Leng, A. Ohmura, L. N. Anh, F. Ishikawa, T. Naka, Y. K. Huang, A. de Visser, *JOURNAL OF PHYSICS-CONDENSED MATTER* **2019**, *32*, 25603.
[97] H. Leng, C. Paulsen, Y. K. Huang, A. de Visser, *PHYSICAL REVIEW B* **2017**, *96*, 220506.
[98] S. Teknowijoyo, N. H. Jo, M. S. Scheurer, M. A. Tanatar, K. Cho, S. L. Bud'ko, P. P. Orth, P. C. Canfield, R. Prozorov, *PHYSICAL REVIEW B* **2018**, *98*.
[99] N. P. Armitage, E. J. Mele, A. Vishwanath, *Reviews of Modern Physics* **2018**, *90*, 15001.
[100] M. Sato, Y. Ando, *Reports on Progress in Physics* **2017**, *80*, 76501.
[101] R. C. Xiao, P. L. Gong, Q. S. Wu, W. J. Lu, M. J. Wei, J. Y. Li, H. Y. Lv, X. Luo, P. Tong, X. B. Zhu et al., *PHYSICAL REVIEW B* **2017**, *96*, 75101.
[102] a) A. A. Soluyanov, D. Gresch, Z. Wang, Q. Wu, M. Troyer, X. Dai, B. A. Bernevig, *NATURE* **2015**, *527*, 495; b) S.-Y. Xu, C. Liu, S. K. Kushwaha, R. Sankar, J. W. Krizan, I. Belopolski, M. Neupane, G. Bian, N. Alidoust, T.-R. Chang et al., *Science* **2015**, *347*, 294.
[103] S. M. Young, S. Zaheer, J. C. Y. Teo, C. L. Kane, E. J. Mele, A. M. Rappe, *Physical Review Letters* **2012**, *108*, 140405.
[104] A. A. Puretzky, A. D. Oyedele, K. Xiao, A. V. Haglund, B. G. Sumpter, D. Mandrus, D. B. Geohegan, L. Liang, *2D Materials* **2018**, *5*, 35016.
[105] Y.-S. Lan, Q. Lu, C.-E. Hu, X.-R. Chen, Q.-F. Chen, *Applied Physics A* **2018**, *125*, 33.
[106] W. Lei, B. Cai, H. Zhou, G. Heymann, X. Tang, S. Zhang, X. Ming, *NANOSCALE* **2019**.
[107] L.-H. Zeng, Di Wu, S.-H. Lin, C. Xie, H.-Y. Yuan, W. Lu, S. P. Lau, Y. Chai, L.-B. Luo, Z.-J. Li et al., *Advanced Functional Materials* **2019**, *29*, 1806878.
[108] M. Sun, J.-P. Chou, L. Shi, J. Gao, A. Hu, W. Tang, G. Zhang, *ACS Omega* **2018**, *3*, 5971.
[109] G. Zhang, M. Amani, A. Chaturvedi, C. Tan, J. Bullock, X. Song, H. Kim, D.-H. Lien, M. C. Scott, H. Zhang et al., *Applied Physics Letters* **2019**, *114*, 253102.
[110] E. Li, D. Wang, P. Fan, R. Zhang, Y.-Y. Zhang, G. Li, J. Mao, Y. Wang, X. Lin, S. Du et al., *Nano Research* **2018**, *11*, 5858.
[111] A. Raja, A. Chaves, J. Yu, G. Arefe, H. M. Hill, A. F. Rigosi, T. C. Berkelbach, P. Nagler, C. Schueller, T. Korn et al., *Nature Communications* **2017**, *8*.
[112] A. L. Hsu, P. K. Herring, N. M. Gabor, S. Ha, Y. C. Shin, Y. Song, M. Chin, M. Dubey, A. P. Chandrakasan, J. Kong et al., *NANO LETTERS* **2015**, *15*, 7211.
[113] T. Walmsley, K. Andrews, T. Wang, A. Haglund, U. Rijal, A. Bowman, D. Mandrus, Z. Zhou, Y. Xu, *NANOSCALE* **2019**.
[114] Y. Jing, Y. Ma, Y. Wang, Y. Li, T. Heine, *Chemistry A European Journal* **2017**, *23*, 13612.
[115] Y. Jiao, F. Ma, L. Zhou, Y. H. Ng, J. Bell, S. Tretiak, A. Du, *Materials Today Energy* **2018**, *7*, 136.
[116] C. Tang, C. Zhang, S. K. Matta, Y. Jiao, K. Ostrikov, T. Liao, L. Kou, A. Du, *JOURNAL OF PHYSICAL CHEMISTRY C* **2018**, *122*, 21927.
[117] R. Dovesi, A. Erba, R. Orlando, C. M. Zicovich-Wilson, B. Civalleri, L. Maschio, M. Rérat, S. Casassa, J. Baima, S. Salustro et al., *Wiley Interdisciplinary Reviews: Computational Molecular Science* **2018**, *8*, e1360.
[118] V. Blum, R. Gehrke, F. Hanke, P. Havu, V. Havu, X. Ren, K. Reuter, M. Scheffler, *Computer Physics Communications* **2009**, *180*, 2175.
[119] T. A. Bither, P. C. Donohue, H. S. Young, *JOURNAL OF SOLID STATE CHEMISTRY* **1971**, *3*, 300.
[120] S. Bhan, T. Gödecke, K. Schubert, *Journal of the Less Common Metals* **1969**, *19*, 121.

ChemArxiv.pdf (1.20 MiB) view on ChemRxiv • download file

Supporting Information: Two-dimensional Noble-Metal Chalcogenides and Phoshochalcogenides

Roman Kempt[1], Agnieszka Kuc[2], and Thomas Heine[1]

[1]Faculty of Chemistry and Food Chemistry, TU Dresden
[2]Institute of Resource Ecology, Helmholtz-Zentrum Dresden-Rossendorf

November 21, 2019

Contents

1 Charge Analysis **3**

2 Computational Method **16**

3 Literature Data and Comparison to this Study **17**
3.1 Experimental Structure Parameters 17
3.2 Calculated Structure Parameters 18

List of Figures

1 Hirshfeld-I charges at the PBE0 level of theory for the bulk compounds in three polytypes. 3
2 Band structures and densities of states (DOS in arbitrary units) of PdS_2 in the $2O$ type for different layer numbers. 4
3 Band structures and densities of states (DOS in arbitrary units) of $PdSe_2$ in the $2O$ type for different layer numbers. 4
4 Band structures and densities of states (DOS in arbitrary units) of high pressure phases of PdS_2 and $PdSe_2$. 4
5 Band structures and densities of states (DOS in arbitrary units) of PtS_2 in the $1T$ type for different layer numbers. 5
6 Band structures and densities of states (DOS in arbitrary units) of $PtSe_2$ in the $1T$ type for different layer numbers. 5
7 Band structures and densities of states (DOS in arbitrary units) of $PtTe_2$ in the $1T$ type for different layer numbers. 5
8 Band structures and densities of states (DOS in arbitrary units) of $PtSe_2$ in the $2H$ type for different layer numbers. 6
9 Band structures and densities of states (DOS in arbitrary units) of $PtSe_2$ in the $2H$ type for different layer numbers. 6
10 Calculated Raman spectra of PtX_2 in the $1T$-type and $2H$-type. $2H$-PtS_2 is considered dynamically instable due to imaginary frequencies. 7
11 Band structures and densities of states of $PdTe_2$ in the $1T$ type for different layer numbers. 8
12 Band structures and densities of states (DOS in arbitrary units) of $PdTe_2$, which is stable in the $2O$ type for fewer layer numbers and as pyrite-phase in the bulk. 8
13 Illustration of the $2O$ bulk Raman modes with A_g symmetry. 9
14 Illustration of the $2O$ bulk Raman modes with B_{1g} symmetry. 10

15 Calculated Raman spectra of PdX_2 in the 2O-type and 1T-type. For metallic systems, intensities cannot be calculated reliably and modes with low intensities were indicated in gray. Bulk 2O-$PdTe_2$ is identical to the pyrite-type. 11
16 Calculated IR spectra of NMDCs in various polytypes. 12
17 Band structures and densities of states (DOS in arbitrary units) of PdS_2 in the 1T type for different layer numbers. 12
18 Band structures and densities of states (DOS in arbitrary units) of $PdSe_2$ in the 1T type for different layer numbers. 13
19 Band structures and densities of states (DOS in arbitrary units) of PdPS for different layer numbers. 13
20 Band structures and densities of states (DOS in arbitrary units) of PdPSe for different layer numbers. 13
21 Calculated Raman spectra of PdPS and PdPSe for different layer numbers. . . . 14

List of Tables

1 Calculated Raman frequencies of bulk PdPS and PdPSe. 15
2 Experimental data on bulk NMDCs and phosphides. Lattice parameters (a, b, c) are given in Angström Å, angles (α, β, γ) in degrees, conventional unit cell volume V in $Å^3$, and band gaps Δ in eV. 17
3 Comparison of calculated and experimental lattice parameters for different methods from literature and this work (∗) for PdS_2. Cr17 refers to Crystal17, VASP to *Vienna Ab Initio Simulation Package*, and QE to *Quantum Espresso* PAW represents projector augmented waves, LCAO refers to linear combination of atomic orbitals, TMNCPP to Troullier-Martins type norm-conserving pseudopotentials. For details on the method please refer to the reference. MAD is the mean average deviation in %. 18
4 Comparison of calculated and experimental lattice parameters for different methods from literature and this work (∗) for $PdSe_2$. Cr17 refers to Crystal17, VASP to *Vienna Ab Initio Simulation Package*, and QE to *Quantum Espresso* PAW represents projector augmented waves, LCAO refers to linear combination of atomic orbitals, TMNCPP to Troullier-Martins type norm-conserving pseudopotentials. For details on the method please refer to the reference. MAD is the mean average deviation in %. 18
5 Comparison of calculated and experimental lattice parameters for different methods from literature and this work (∗) for $PdTe_2$. Cr17 refers to Crystal17, VASP to *Vienna Ab Initio Simulation Package*, and QE to *Quantum Espresso* PAW represents projector augmented waves, LCAO refers to linear combination of atomic orbitals, TMNCPP to Troullier-Martins type norm-conserving pseudopotentials. For details on the method please refer to the reference. MAD is the mean average deviation in %. 19
6 Comparison of calculated and experimental lattice parameters for different methods from literature and this work (∗) for PdPS, PdP_2, and PtX_2. Cr17 refers to Crystal17, VASP to *Vienna Ab Initio Simulation Package*, and QE to *Quantum Espresso* PAW represents projector augmented waves, LCAO refers to linear combination of atomic orbitals, TMNCPP to Troullier-Martins type norm-conserving pseudopotentials. For details on the method please refer to the reference. MAD is the mean average deviation in %. 20

1 Charge Analysis

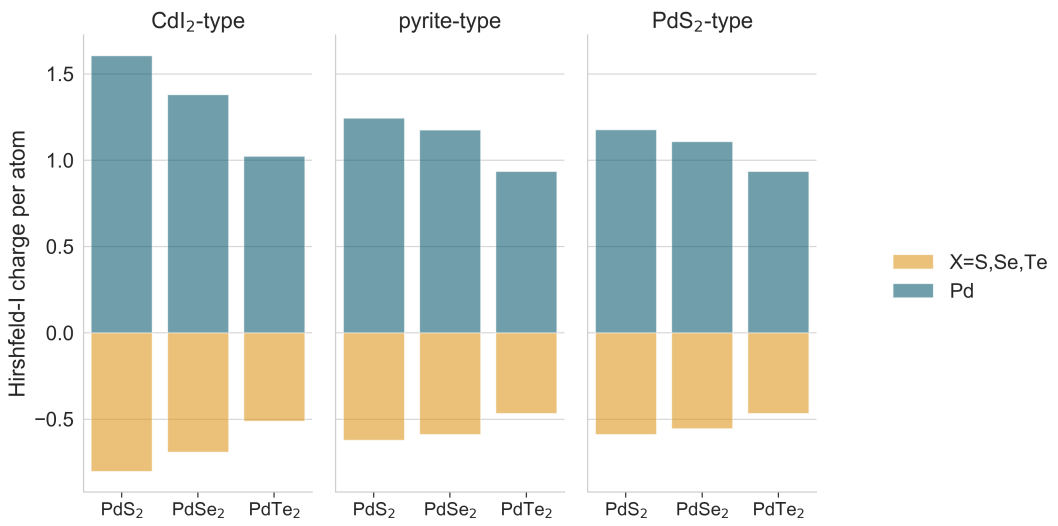


Figure 1: Hirshfeld-I charges at the PBE0 level of theory for the bulk compounds in three polytypes.

The Hirshfeld charge analysis shows a large charge transfer (corresponding to more ionic bonding) in the $1T$ structures of PdS_2 and $PdSe_2$ in comparison to their pyrite-type structure and the derived PdS_2-type structure. This can be interpreted as a higher oxidation state in the $1T$ phase. In order to lower their oxidation state, the chalcogens undergo dimer formation, which leads to the pyrite-type and PdS_2-type structures. In the case of $PdTe_2$, the charge transfer between the $1T$ and pyrite structures has similar magnitude, corresponding to no change in the oxidation state. Since Te-Te dimer formation is less favorable, $PdTe_2$ stays in the $1T$ structure.

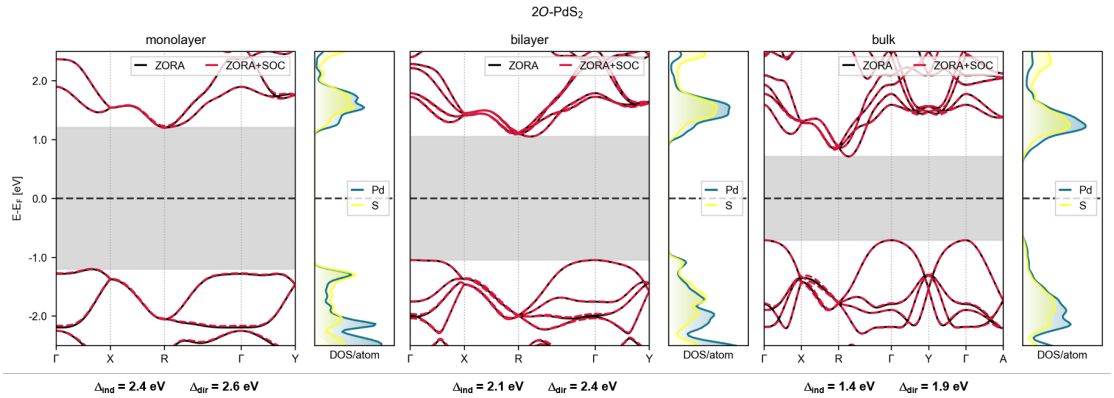


Figure 2: Band structures and densities of states (DOS in arbitrary units) of PdS_2 in the 2*O* type for different layer numbers.

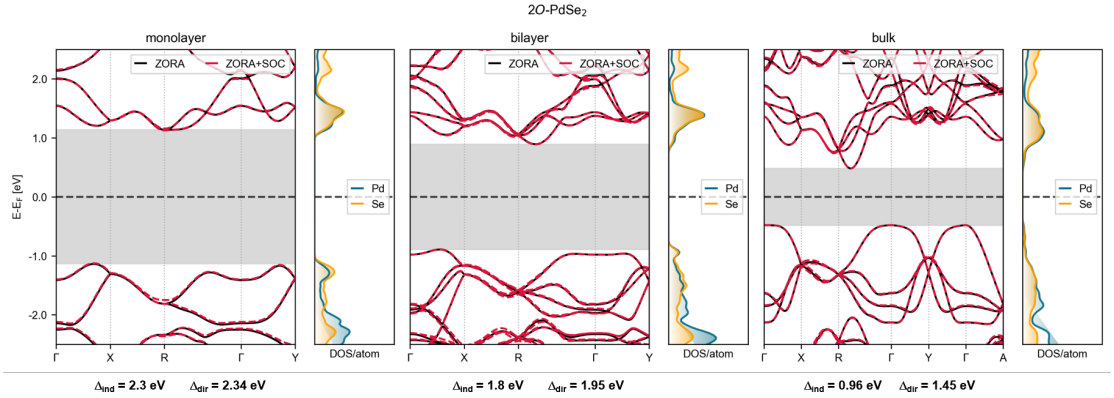


Figure 3: Band structures and densities of states (DOS in arbitrary units) of $PdSe_2$ in the 2*O* type for different layer numbers.

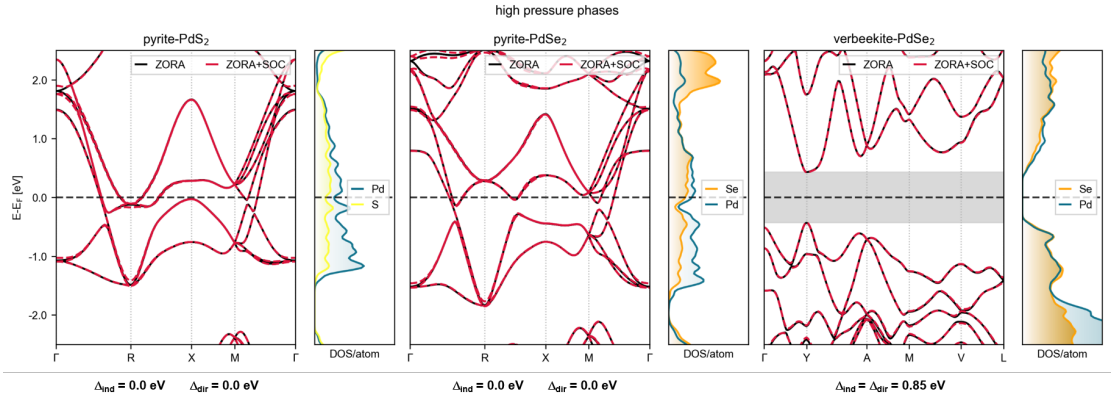


Figure 4: Band structures and densities of states (DOS in arbitrary units) of high pressure phases of PdS_2 and $PdSe_2$.

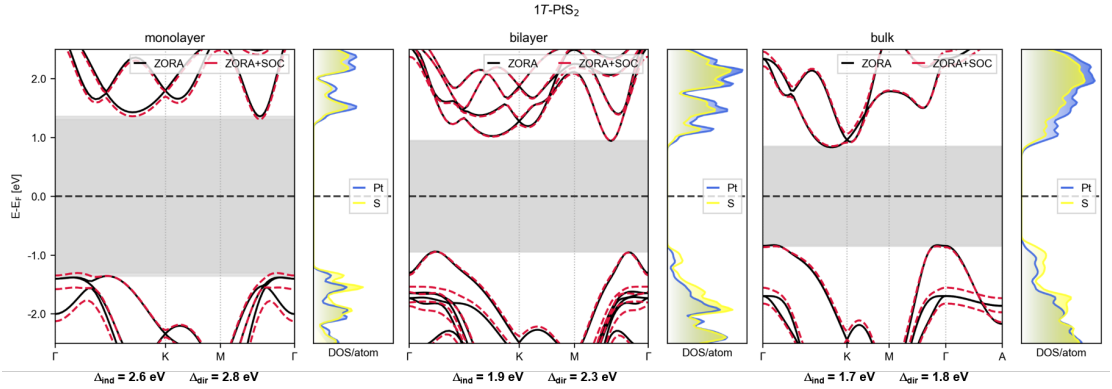


Figure 5: Band structures and densities of states (DOS in arbitrary units) of PtS_2 in the 1T type for different layer numbers.

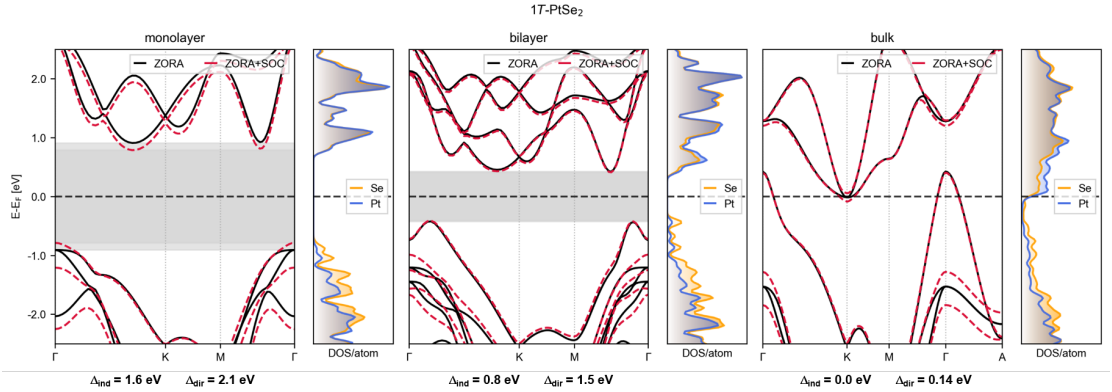


Figure 6: Band structures and densities of states (DOS in arbitrary units) of $PtSe_2$ in the 1T type for different layer numbers.

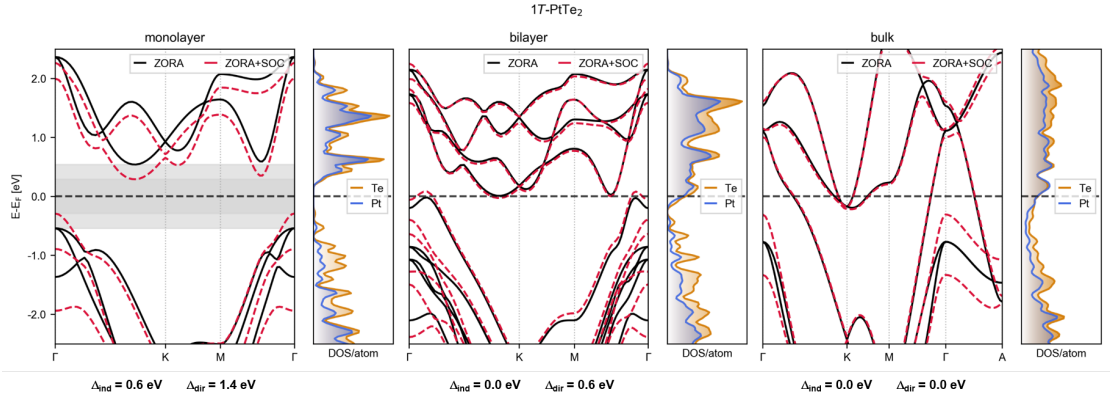


Figure 7: Band structures and densities of states (DOS in arbitrary units) of $PtTe_2$ in the 1T type for different layer numbers.

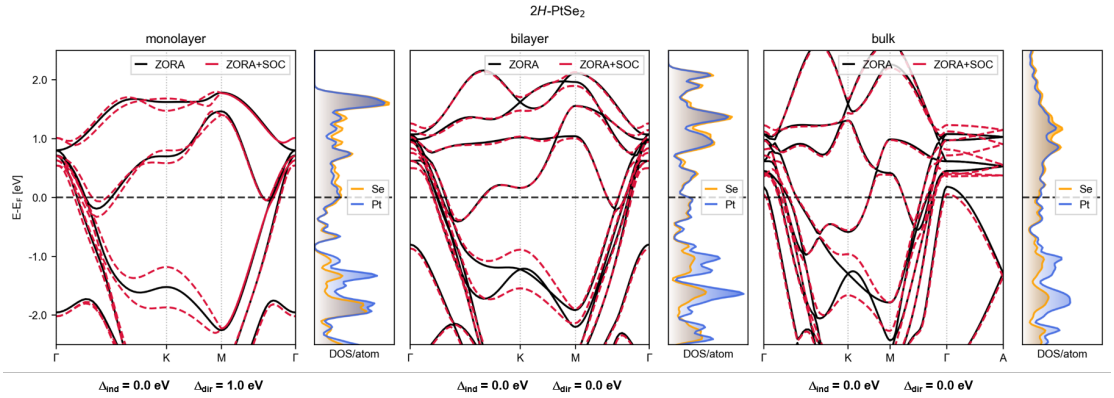


Figure 8: Band structures and densities of states (DOS in arbitrary units) of $PtSe_2$ in the $2H$ type for different layer numbers.

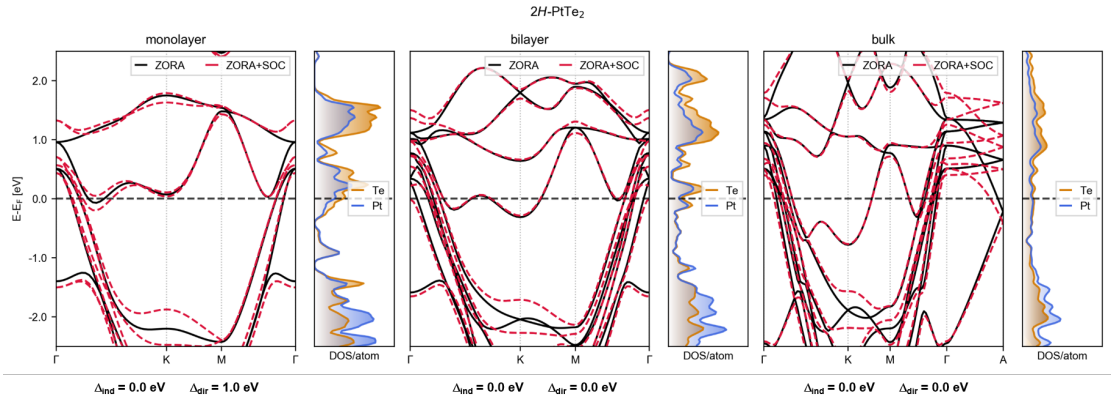


Figure 9: Band structures and densities of states (DOS in arbitrary units) of $PtSe_2$ in the $2H$ type for different layer numbers.

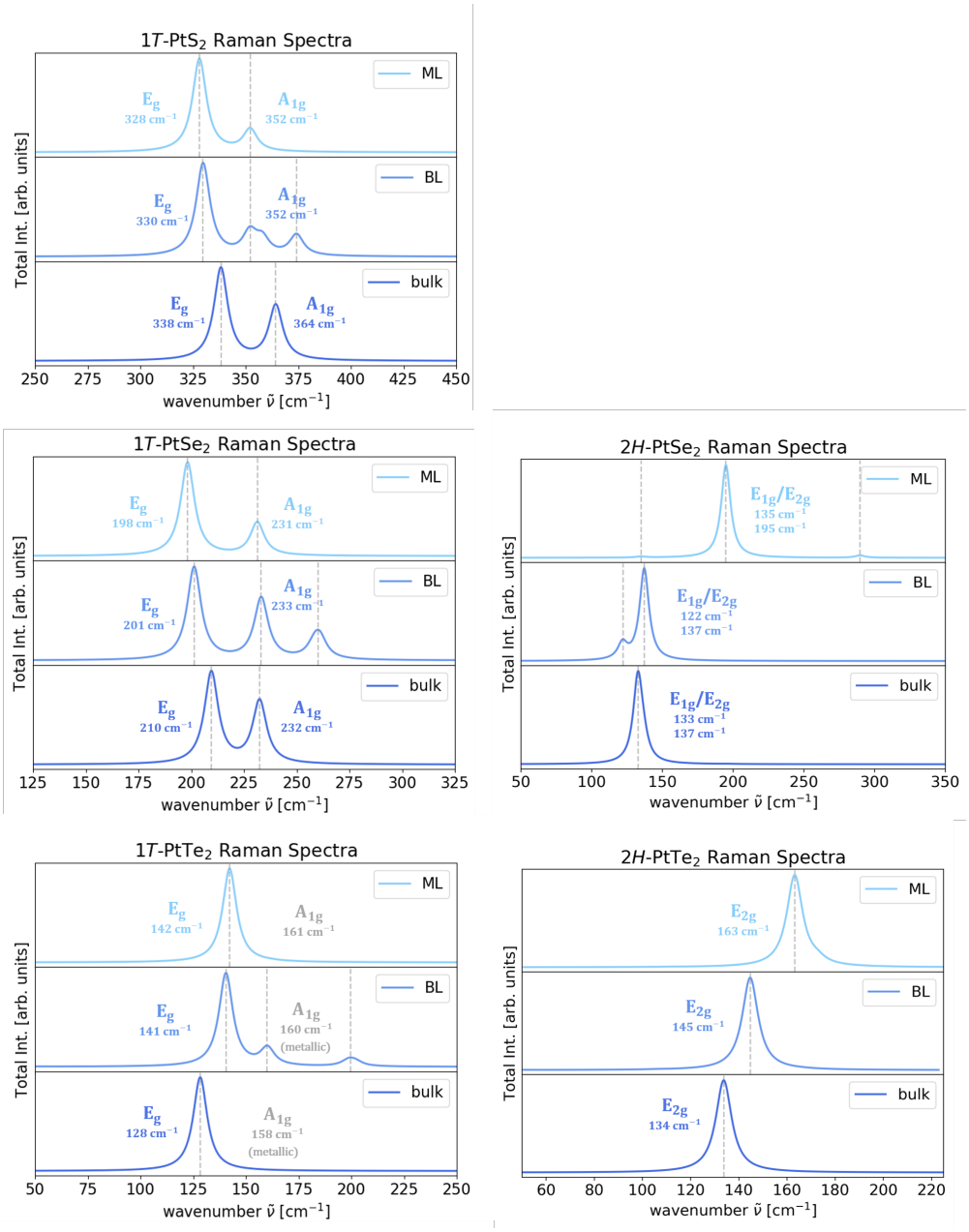


Figure 10: Calculated Raman spectra of PtX_2 in the $1T$-type and $2H$-type. $2H$-PtS_2 is considered dynamically instable due to imaginary frequencies.

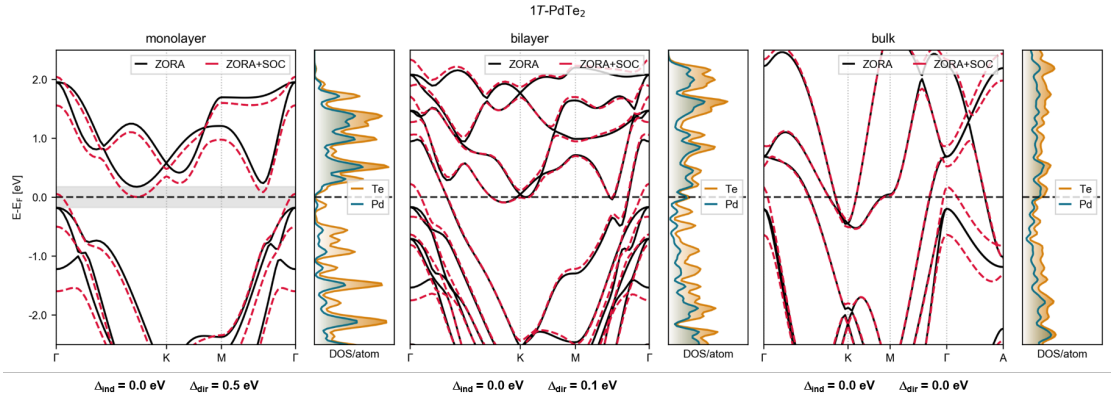


Figure 11: Band structures and densities of states of $PdTe_2$ in the $1T$ type for different layer numbers.

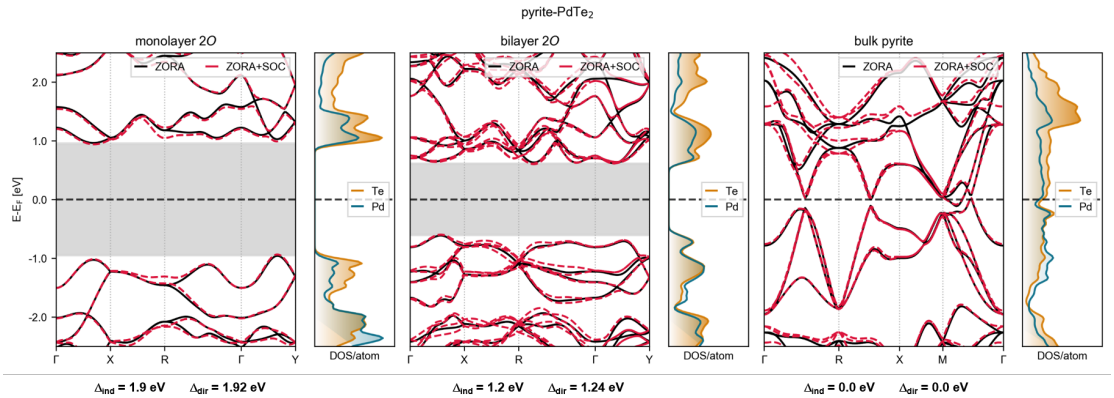


Figure 12: Band structures and densities of states (DOS in arbitrary units) of $PdTe_2$, which is stable in the $2O$ type for fewer layer numbers and as pyrite-phase in the bulk.

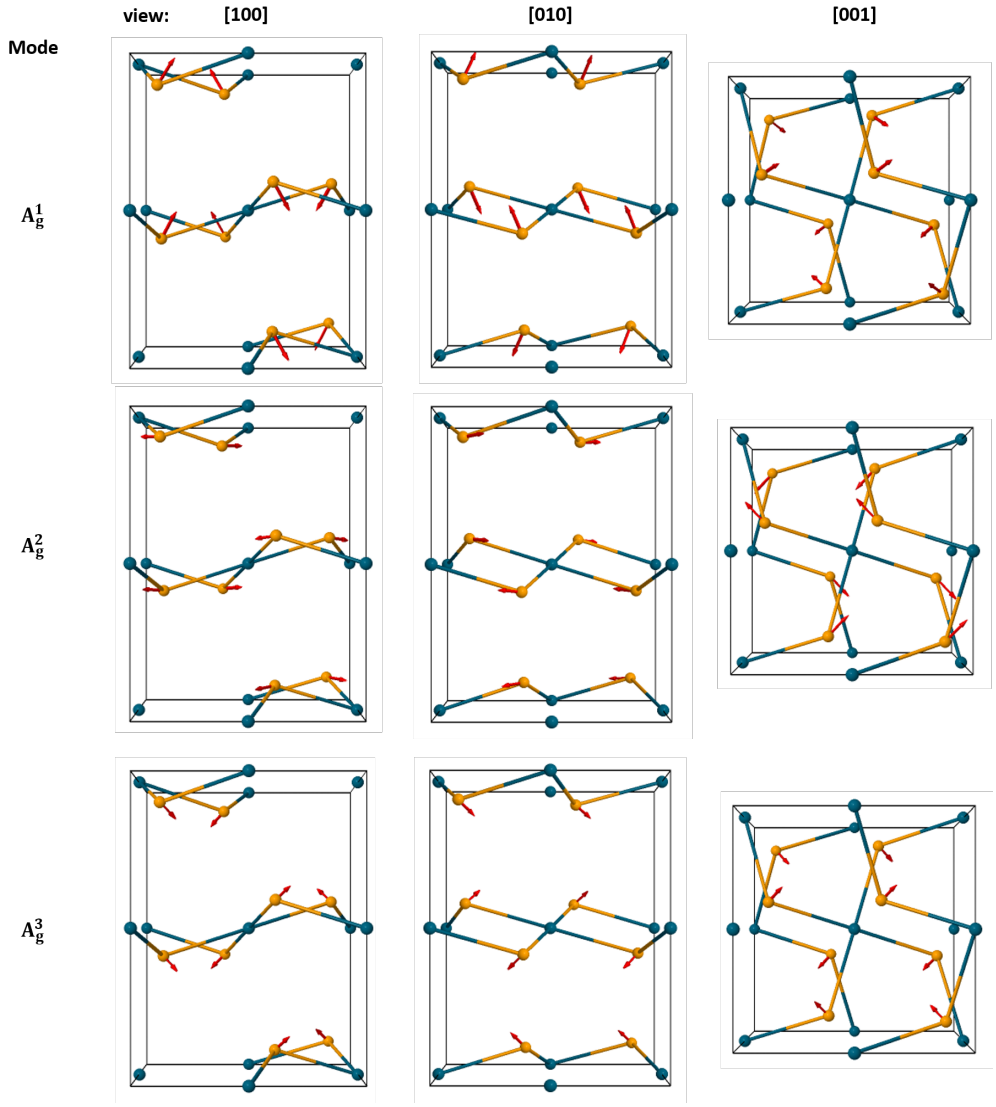


Figure 13: Illustration of the $2O$ bulk Raman modes with A_g symmetry.

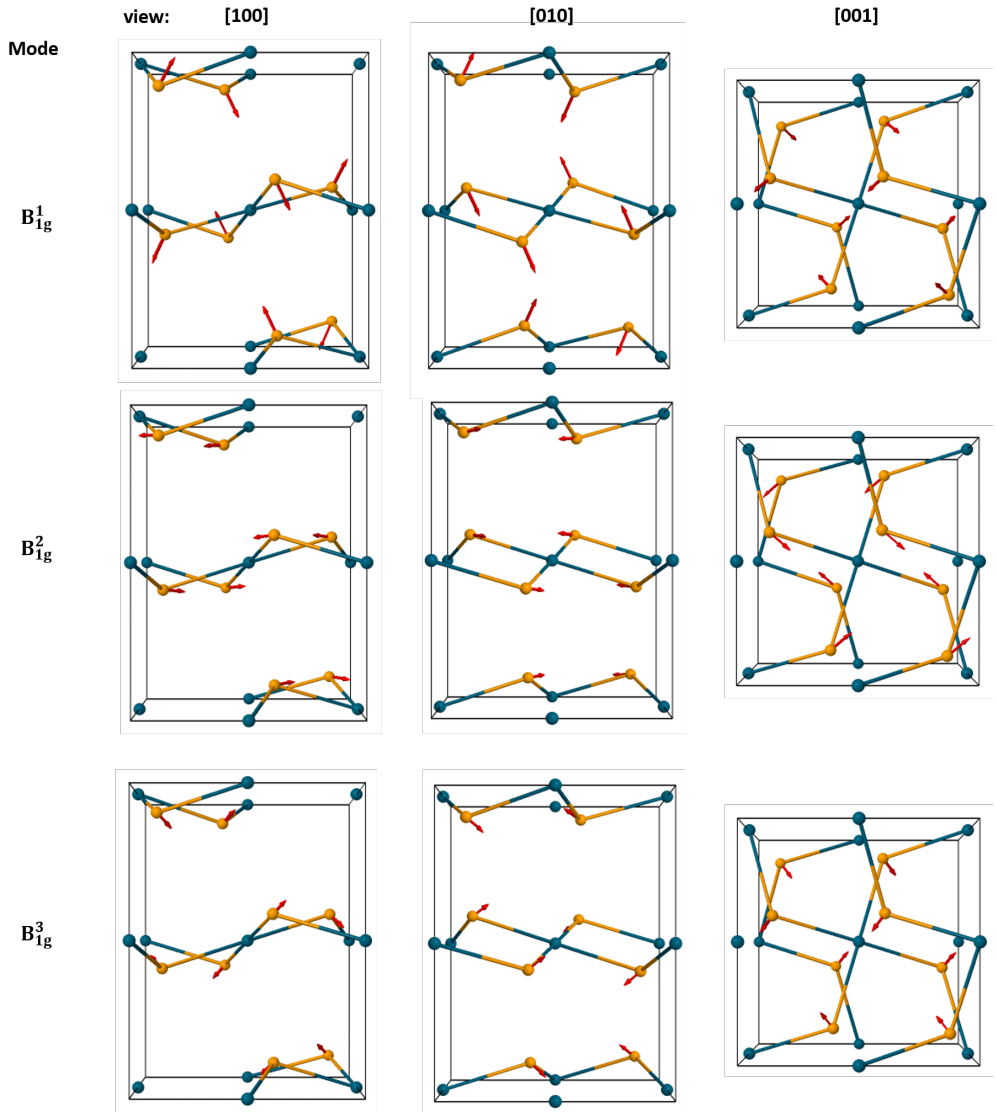


Figure 14: Illustration of the $2O$ bulk Raman modes with B_{1g} symmetry.

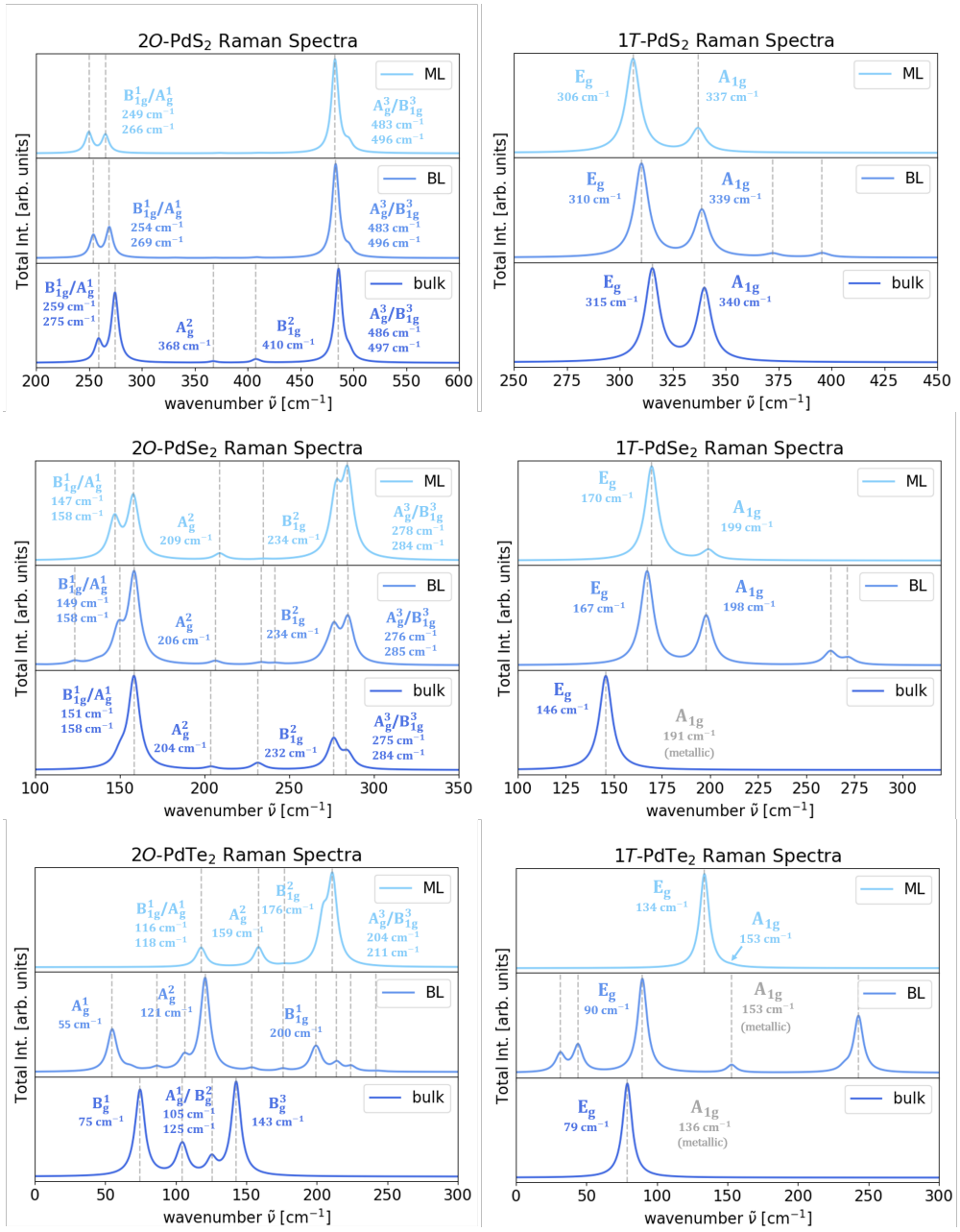


Figure 15: Calculated Raman spectra of PdX_2 in the 2*O*-type and 1*T*-type. For metallic systems, intensities cannot be calculated reliably and modes with low intensities were indicated in gray. Bulk 2*O*-$PdTe_2$ is identical to the pyrite-type.

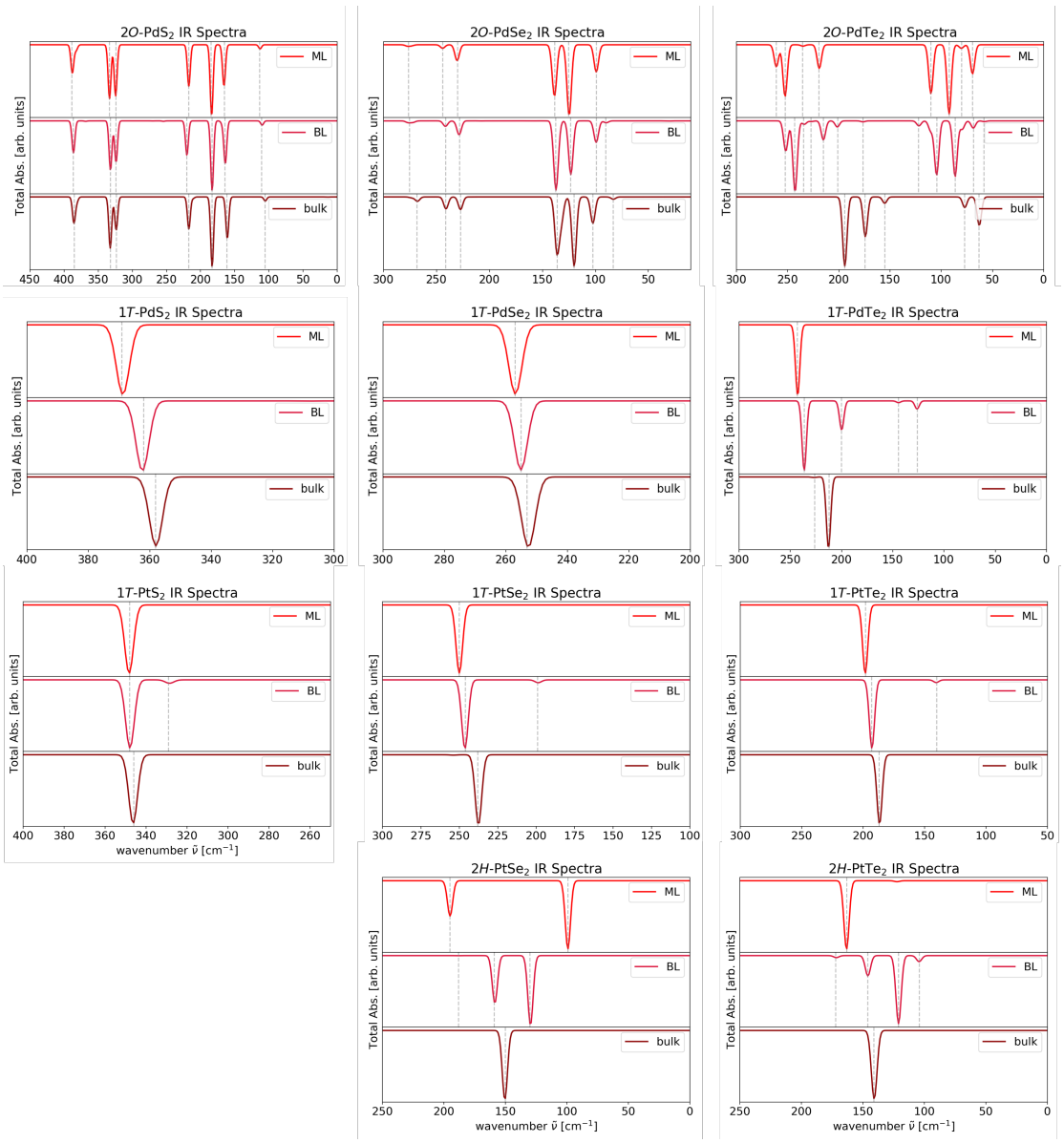


Figure 16: Calculated IR spectra of NMDCs in various polytypes.

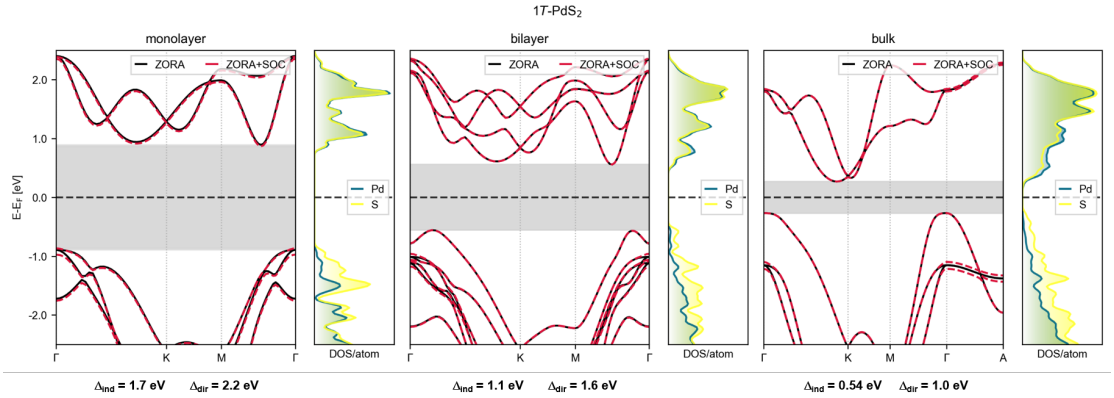


Figure 17: Band structures and densities of states (DOS in arbitrary units) of PdS_2 in the 1*T* type for different layer numbers.

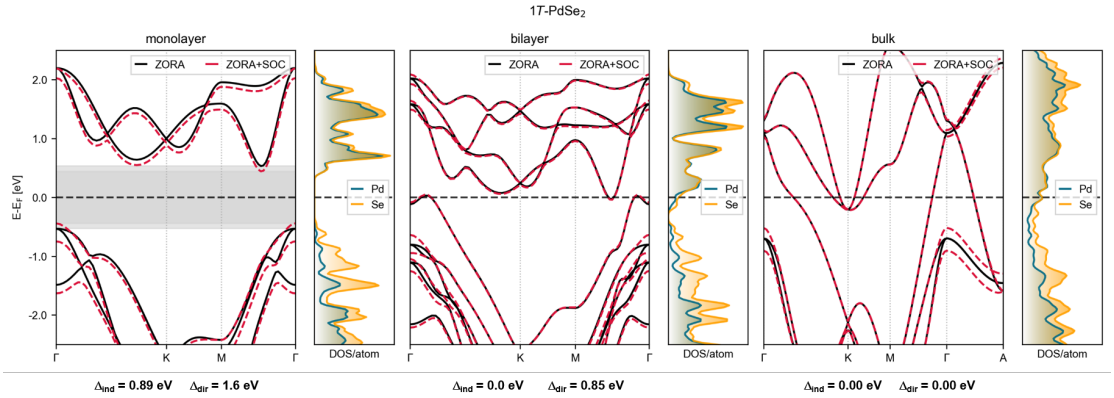


Figure 18: Band structures and densities of states (DOS in arbitrary units) of $PdSe_2$ in the $1T$ type for different layer numbers.

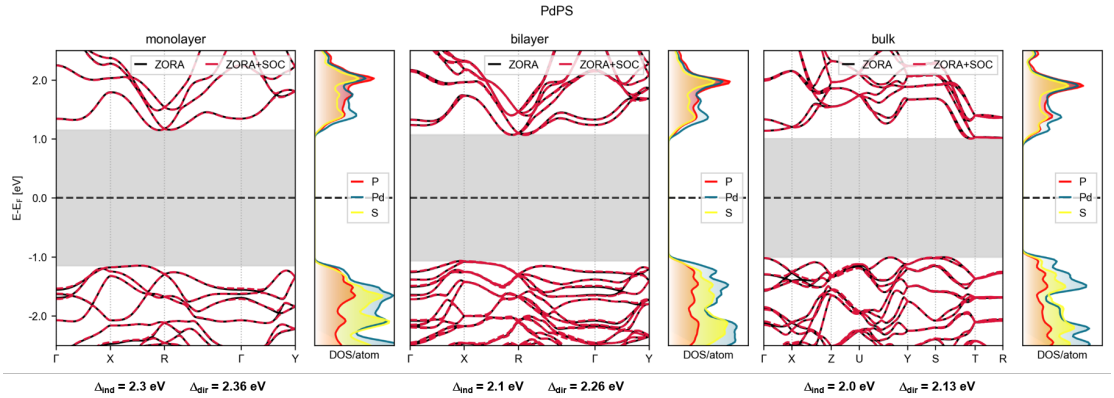


Figure 19: Band structures and densities of states (DOS in arbitrary units) of PdPS for different layer numbers.

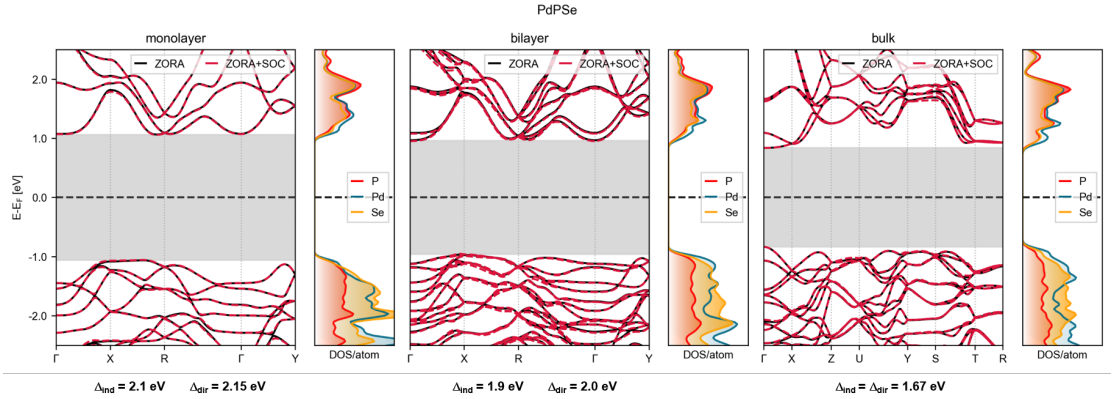


Figure 20: Band structures and densities of states (DOS in arbitrary units) of PdPSe for different layer numbers.

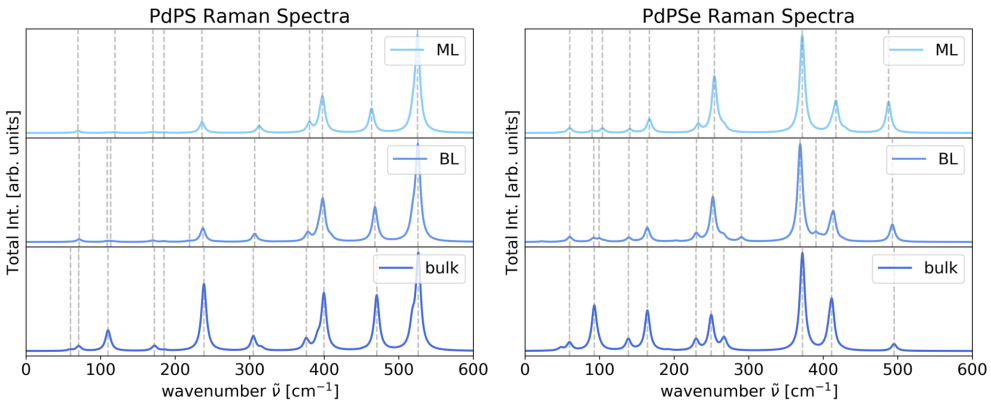


Figure 21: Calculated Raman spectra of PdPS and PdPSe for different layer numbers.

Table 1: Calculated Raman frequencies of bulk PdPS and PdPSe.

bulk PdPS		bulk PdPSe	
Mode	Freq. [$\tilde{\nu}$]	Mode	Freq. [$\tilde{\nu}$]
B_{1g}	59.15	B_{1g}	48.0
A_g	70.73	A_g	59.7
A_g	110.0	A_g	92.9
B_{2g}	112.4	B_{2g}	98.7
A_g	172.3	B_{1g}	98.9
B_{2g}	185.6	B_{3g}	137.6
A_g	238.6	A_g	138.6
B_{2g}	240.3	A_g	164.2
A_g	304.9	A_g	229.2
B_{1g}	315.8	B_{3g}	231.1
A_g	375.6	A_g	249.7
B_{3g}	377.3	B_{3g}	251.0
B_{1g}	390.0	B_{2g}	265.6
B_{2g}	391.3	B_{1g}	267.8
A_g	399.7	A_g	372.1
A_g	470.5	B_{1g}	406.4
B_{2g}	518.3	B_{2g}	407.8
A_g	526.3	A_g	411.6
-	-	A_g	495.1

2 Computational Method

Due to the importance of electron correlation, common DFT approaches, such as PBE-D3 or PBE-MBD, easily misjudge phase stabilities in the case of the Noble-Metal Dichalcogenides (NMDCs). [1–7] The performance of different approaches is summarized in Tables 3, 4, 5 and 6. To obtain reliable predictions, we employ the PBE0 functional [8] to calculate all structural features, such as stabilities, ground-state structures, and vibrational spectra. We show that this approach yields mean average deviations of ≈5 % from experimental structures.

In detail, we performed full relaxation of lattice vectors and atomic positions with Crystal17 [9] and FHI-AIMS [10] (the latter for calculations including many-body-dispersion). We started from experimental structures where available (see Table 2). Hypothetical structures were varied with respect to their lattice parameters and subsequently re-optimised. Calculations in Crystal17 were generally performed on a triple-ζ valence polarisation (TZVP) basis. [11] In case of Pt, only a double-ζ valence polarisation basis was available. [12] In FHI-AIMS, the *tight* tier 2 basis sets were used. All relaxations were performed on sufficiently large k-grids of at least 18×18(×18) k-points, where for metallic systems the sampling was increased up to 24×24(×24). In Crystal17, the structures were optimised till the root-mean-square deviations of the gradients were smaller than 0.00003 a.u. and of the estimated displacements smaller than 0.00012 a.u., while the energy change between subsequent SCF cycles was optimised till below 10^{-8} a.u. In case of metallic systems, the Fermi-surface was smeared by a finite temperature of 0.02 a.u. In FHI-AIMS, all forces were relaxed till below 5×10^{-3}. All optimised structures showed non-negative Γ-point frequencies.

For optimisation, we investigated the GGA-type functional by Perdew, Burke and Ernzerhof (PBE) [13] including different corrections for the dispersion energy, such as DFT-D by Grimme et al. [14–16], Becke-Johnson damping (BJ) [17], and the many-body-dispersion correction (MBD). [18, 19] Furthermore, we employed the hybrid functional PBE0 [8] and the range-separated hybrid functional from Heyd, Scuseria and Ernzerhof HSE06 [20–22]. The hybrid functionals were the only functionals that correctly reproduced experimental phase stabilities in our investigations.

Electronic structure calculations, including band structures and densities of states, were carried out in FHI-AIMS including full treatment of relativistic effects through the Zeroth Order Regular Approximation (ZORA) and Spin-Orbit Coupling (SOC) with the HSE06 functional. [22] Raman and IR spectra were predicted employing the Coupled Perturbed Kohn-Sham approach [23–25] on optimised structures as implemented in Crystal17 [9] with PBE0.

3 Literature Data and Comparison to this Study

3.1 Experimental Structure Parameters

Table 2: Experimental data on bulk NMDCs and phosphides. Lattice parameters (a, b, c) are given in Angström Å, angles (α, β, γ) in degrees, conventional unit cell volume V in Å^3, and band gaps Δ in eV.

System	Type	a	b	c	α	β	γ	V	Δ	Ref.
PdS_2	PdS_2	5.460	5.416	7.531	90	90	90	228	0.70	[26, 27]
PdS_2	PdS_2-II	5.520	5.551	7.202	90	90	90	221	-	[28]
$PdSe_2$	PdS_2	5.741	5.866	7.691	90	90	90	259	0.50	[26, 27, 29]
$PdSe_2$	Marcasite	4.873	6.013	3.930	90	90	90	115	-	[30]
$PdSe_2$	Pyrite	6.100	6.100	6.100	90	90	90	227	0.0	[30]
$PdSe_2$	Verbeekite	10.93	4.154	6.710	90	125	90	248	-	[31]
$PdTe_2$	CdI_2	4.037	4.037	5.126	90	90	120	72.3	0.0	[27, 32]
PdP_2	PdP_2	6.779	5.857	5.874	90	122	90	99.1	-	[33]
PdPS	PdPS	13.31	5.678	5.693	90	90	90	430	0.65	[34, 35]
PdPSe	PdPS	13.57	5.824	5.856	90	90	90	463	0.15	[34, 35]
PdSSe	PdS_2	5.595	5.713	7.672	90	90	90	245	0.70	[27]
PdSeTe	CdI_2	3.900	3.900	4.980	90	90	120	65.6	0.0	[27]
PtS_2	CdI_2	3.543	3.543	5.039	90	90	120	54.8	0.70	[27, 36]
$PtSe_2$	CdI_2	3.728	3.728	5.081	90	90	120	61.2	0.0	[36, 37]
$PtTe_2$	CdI_2	4.026	4.026	5.221	90	90	120	71.3	0.0	[27, 36]

3.2 Calculated Structure Parameters

We define the MAD as:

$$MAD = \sqrt{\left(\frac{\Delta a}{a}\right)^2 + \left(\frac{\Delta b}{b}\right)^2 + \left(\frac{\Delta c}{c}\right)^2 + \left(\frac{\Delta \alpha}{\alpha}\right)^2 + \left(\frac{\Delta \beta}{\beta}\right)^2 + \left(\frac{\Delta \gamma}{\gamma}\right)^2} \cdot 100\% \qquad (1)$$

Where the reference is the available experimental data.

Table 3: Comparison of calculated and experimental lattice parameters for different methods from literature and this work (∗) for PdS_2. Cr17 refers to Crystal17, VASP to *Vienna Ab Initio Simulation Package*, and QE to *Quantum Espresso* PAW represents projector augmented waves, LCAO refers to linear combination of atomic orbitals, TMNCPP to Troullier-Martins type norm-conserving pseudopotentials. For details on the method please refer to the reference. MAD is the mean average deviation in %.

System	Structure	a	b	c	α	β	γ	MAD	Method	Ref.
PdS_2	PdS_2	5.465	5.538	7.525	90	90	90	2.26	LDA+PW/PAW(VASP)	[38]
PdS_2	PdS_2	5.485	5.582	7.661	90	90	90	3.55	PBE/LCAO(Cr17)	∗
PdS_2	PdS_2	5.475	5.578	7.697	90	90	90	3.73	PBE-D2/LCAO(Cr17)	∗
PdS_2	PdS_2	5.851	5.841	5.840	90	90	90	24.84	PBE-D3/LCAO(Cr17)	∗
PdS_2	PdS_2	5.829	5.836	5.822	90	90	90	24.92	PBE-D3(BJ)/LCAO(Cr17)	∗
PdS_2	PdS_2	5.644	5.694	6.773	90	90	90	11.79	PBE-MBD/LCAO(AIMS)	∗
PdS_2	PdS_2	5.429	5.527	7.894	90	90	90	5.27	HSE06/LCAO(Cr17)	∗
PdS_2	PdS_2	5.424	5.494	7.083	90	90	90	6.16	HSE06-D3(BJ)/LCAO(Cr17)	∗
PdS_2	PdS_2	5.416	5.521	7.946	90	90	90	5.9	PBE0/LCAO(Cr17)	∗
PdS_2	CdI_2	3.483	3.483	5.226	90	90	120	-	PBE0/LCAO(Cr17)	∗
PdS_2	Pyrite	5.855	5.855	5.855	90	90	90	-	PBE0/LCAO(Cr17)	∗
PdS_2	Marcasite	4.793	5.599	3.870	90	90	90	-	PBE0/LCAO(Cr17)	∗

Table 4: Comparison of calculated and experimental lattice parameters for different methods from literature and this work (∗) for $PdSe_2$. Cr17 refers to Crystal17, VASP to *Vienna Ab Initio Simulation Package*, and QE to *Quantum Espresso* PAW represents projector augmented waves, LCAO refers to linear combination of atomic orbitals, TMNCPP to Troullier-Martins type norm-conserving pseudopotentials. For details on the method please refer to the reference. MAD is the mean average deviation in %.

System	Structure	a	b	c	α	β	γ	MAD	Method	Ref.
$PdSe_2$	PdS_2	5.875	5.982	7.72	90	90	90	3.08	LDA+PW/PAW(VASP)	[39]
$PdSe_2$	PdS_2	5.866	6.000	7.356	90	90	90	5.38	LDA+PW/PAW(VASP)	[38]
$PdSe_2$	PdS_2	5.773	5.856	7.384	90	90	90	4.03	DFPTLDA-PZ(CASTEP)	[40]
$PdSe_2$	PdS_2	6.110	6.100	6.120	90	90	90	21.78	LDA/PAW(VASP)	[1]
$PdSe_2$	PdS_2	5.790	5.940	8.480	90	90	90	10.37	PBE/PAW(VASP)	[1]
$PdSe_2$	PdS_2	6.200	6.190	6.210	90	90	90	21.57	DFT-D2/PAW(VASP)	[1]
$PdSe_2$	PdS_2	5.900	6.050	8.470	90	90	90	10.96	vdW-DF/PAW(VASP)	[1]
$PdSe_2$	PdS_2	6.010	6.150	8.340	90	90	90	10.8	vdW-DF2/PAW(VASP)	[1]
$PdSe_2$	PdS_2	5.805	5.990	7.950	90	90	90	4.41	optPBE/PAW(VASP)	[1]
$PdSe_2$	PdS_2	6.220	6.220	6.230	90	90	90	21.61	optB86b/PAW(VASP)	[1]
$PdSe_2$	PdS_2	5.850	5.970	7.630	90	90	90	2.72	optB88/PAW(VASP)	[1]
$PdSe_2$	PdS_2	6.090	6.100	6.100	90	90	90	21.93	LDA/PAW(QE)	[1]
$PdSe_2$	PdS_2	5.800	5.950	8.650	90	90	90	12.59	PBE/PAW(QE)	[1]
$PdSe_2$	PdS_2	5.790	5.920	7.700	90	90	90	1.26	DFT-D2/PAW(QE)	[1]
$PdSe_2$	PdS_2	5.890	6.050	8.680	90	90	90	13.49	vdw-DF/PAW(QE)	[1]
$PdSe_2$	PdS_2	6.010	6.160	8.470	90	90	90	12.23	vdw-DF2/PAW(QE)	[1]
$PdSe_2$	PdS_2	6.160	6.170	6.170	90	90	90	21.71	C09-DF/PAW(QE)	[1]
$PdSe_2$	PdS_2	6.180	6.170	6.190	90	90	90	21.59	C09-DF2/PAW(QE)	[1]
$PdSe_2$	PdS_2	5.840	5.950	7.490	90	90	90	3.44	optB86b/PAW(QE)	[1]
$PdSe_2$	PdS_2	5.860	5.990	7.710	90	90	90	2.97	optB88/PAW(QE)	[1]
$PdSe_2$	PdS_2	5.840	5.960	7.530	90	90	90	3.15	revB86b/PAW(QE)	[1]
$PdSe_2$	PdS_2	6.100	6.110	6.110	90	90	90	21.89	LDA/TMNCPP(QE)	[1]
$PdSe_2$	PdS_2	5.790	5.950	8.720	90	90	90	13.48	PBE/TMNCPP(QE)	[1]
$PdSe_2$	PdS_2	5.780	5.920	7.770	90	90	90	1.54	DFT-D2/TMNCPP(QE)	[1]
$PdSe_2$	PdS_2	5.900	6.050	8.640	90	90	90	13.03	vdW-DF/TMNCPP(QE)	[1]
$PdSe_2$	PdS_2	5.790	5.950	8.680	90	90	90	12.97	vdW-DF2/TMNCPP(QE)	[1]

$PdSe_2$	PdS_2	6.210	6.220	6.210	90	90	90	21.77	C09-DF/TMNCPP(QE)	[1]
$PdSe_2$	PdS_2	6.220	6.230	6.220	90	90	90	21.77	C09-DF2/TMNCPP(QE)	[1]
$PdSe_2$	PdS_2	5.790	5.950	8.680	90	90	90	12.97	optB86b/TMNCPP(QE)	[1]
$PdSe_2$	PdS_2	5.790	5.950	8.720	90	90	90	13.48	optB88/TMNCPP(QE)	[1]
$PdSe_2$	PdS_2	5.790	5.950	8.690	90	90	90	13.1	revB86b/TMNCPP(QE)	[1]
$PdSe_2$	PdS_2	5.786	5.936	8.608	90	90	90	12.01	PBE/PAW(VASP)	[7]
$PdSe_2$	PdS_2	5.848	5.947	7.758	90	90	90	2.48	DFT-D(TS)/PAW(VASP)	[7]
$PdSe_2$	Verbeekite	11.111	4.015	6.728	90	125.0	90	3.76	DFT-D(TS)/PAW(VASP)	[7]
$PdSe_2$	Verbeekite	11.059	3.902	6.632	90	124.6	90	6.33	DFT-D3(BJ)/PAW(VASP)	[7]
$PdSe_2$	Verbeekite	11.068	3.952	6.686	90	125.1	90	5.04	DFT-D3/PAW(VASP)	[7]
$PdSe_2$	Verbeekite	11.107	3.893	6.628	90	124.5	90	6.64	DFT-D2/PAW(VASP)	[7]
$PdSe_2$	Verbeekite	11.145	3.938	6.666	90	124.3	90	5.66	optB86b-vDW/PAW(VASP)	[7]
$PdSe_2$	Verbeekite	11.146	4.159	6.781	90	124.6	90	2.33	optPBE-vdW/PAW(VASP)	[7]
$PdSe_2$	Verbeekite	11.213	4.203	6.821	90	124.7	90	3.34	optB88-vdW/PAW(VASP)	[7]
$PdSe_2$	Verbeekite	11.468	3.751	6.500	90	124.5	90	11.35	PBEsol/PAW(VASP)	[7]
$PdSe_2$	Verbeekite	11.055	4.153	6.755	90	124.8	90	1.41	PBE/PAW(VASP)	[7]
$PdSe_2$	PdS_2	5.779	5.931	8.495	90	90	90	10.53	PBE/PAW(VASP)	[2]
$PdSe_2$	PdS_2	6.196	6.196	6.193	90	90	90	21.77	PBE-D2/PAW(VASP)	[2]
$PdSe_2$	PdS_2	6.198	6.197	6.192	90	90	90	21.8	PBE-D3(ZP)/PAW(VASP)	[2]
$PdSe_2$	PdS_2	6.179	6.178	6.173	90	90	90	21.82	PBE-D3(BJ)/PAW(VASP)	[2]
$PdSe_2$	PdS_2	6.208	6.210	6.201	90	90	90	21.81	PBE-dDsC/PAW(VASP)	[2]
$PdSe_2$	PdS_2	6.310	6.310	6.303	90	90	90	21.94	optPBE/PAW(VASP)	[2]
$PdSe_2$	PdS_2	6.220	6.221	6.212	90	90	90	21.82	optB86b/PAW(VASP)	[2]
$PdSe_2$	PdS_2	6.268	6.269	6.258	90	90	90	21.88	optB88/PAW(VASP)	[2]
$PdSe_2$	PdS_2	6.512	6.513	6.524	90	90	90	23.07	vdW-DF2/PAW(VASP)	[2]
$PdSe_2$	PdS_2	5.862	5.953	7.59	90	90	90	2.89	PBE-TS/PAW(VASP)	[2]
$PdSe_2$	PdS_2	5.859	5.955	7.591	90	90	90	2.87	PBE-TS(HI)/PAW(VASP)	[2]
$PdSe_2$	PdS_2	5.851	5.947	7.694	90	90	90	2.36	PBE-TS(SCS)/PAW(VASP)	[2]
$PdSe_2$	PdS_2	6.058	6.082	6.688	90	90	90	14.63	PBE/LCAO(Cr17)	*
$PdSe_2$	PdS_2	6.017	6.057	6.825	90	90	90	12.67	PBE-D2/LCAO(Cr17)	*
$PdSe_2$	PdS_2	6.183	6.173	6.19	90	90	90	21.62	PBE-D3/LCAO(Cr7)	*
$PdSe_2$	PdS_2	6.171	6.159	6.166	90	90	90	21.78	PBE-D3(BJ)/LCAO(Cr17)	*
$PdSe_2$	PdS_2	6.234	6.234	6.234	90	90	90	21.73	PBE-MBD/LCAO(AIMS)	*
$PdSe_2$	PdS_2	5.734	5.874	7.998	90	90	90	4.0	HSE06/LCAO(Cr17)	*
$PdSe_2$	PdS_2	5.722	5.830	7.304	90	90	90	5.08	HSE06-D3(BJ)/LCAO(Cr17)	*
$PdSe_2$	PdS_2	5.718	5.864	8.048	90	90	90	4.66	PBE0/LCAO(Cr17)	*
$PdSe_2$	Pyrite	6.194	6.194	6.194	90	90	90	2.67	PBE0/LCAO(Cr17)	*
$PdSe_2$	Marcasite	5.135	5.938	4.06	90	90	90	6.43	PBE0/LCAO(Cr17)	*
$PdSe_2$	Verbeekite	10.850	4.154	6.689	90	125.6	90	0.81	PBE0/LCAO(Cr17)	*
$PdSe_2$	CdI_2	3.734	3.734	4.889	90	90	120	-	PBE0/LCAO(Cr17)	*

Table 5: Comparison of calculated and experimental lattice parameters for different methods from literature and this work (∗) for $PdTe_2$. Cr17 refers to Crystal17, VASP to *Vienna Ab Initio Simulation Package*, and QE to *Quantum Espresso* PAW represents projector augmented waves, LCAO refers to linear combination of atomic orbitals, TMNCPP to Troullier-Martins type norm-conserving pseudopotentials. For details on the method please refer to the reference. MAD is the mean average deviation in %.

System	Structure	a	b	c	α	β	γ	MAD	Method	Ref.
$PdTe_2$	CdI_2	4.097	4.097	5.19	90	90	120	2.44	PBE/PAW(Vasp)	[41]
$PdTe_2$	CdI_2	4.033	4.033	5.231	90	90	120	2.05	PBE/LCAO(Cr17)	*
$PdTe_2$	CdI_2	4.023	4.023	5.206	90	90	120	1.64	PBE-D2/LCAO(Cr17)	*
$PdTe_2$	CdI_2	4.016	4.016	5.034	90	90	120	1.94	PBE-D3/LCAO(Cr17)	*
$PdTe_2$	CdI_2	3.989	3.989	5.069	90	90	120	2.02	PBE-D3(BJ)/LCAO(Cr17)	*
$PdTe_2$	CdI_2	4.077	4.077	5.147	90	90	120	1.46	PBE-MBD/LCAO(AIMS)	*
$PdTe_2$	CdI_2	4.009	4.009	5.184	90	90	120	1.5	HSE06/LCAO(Cr17)	*
$PdTe_2$	CdI_2	3.963	3.963	4.972	90	90	120	3.97	HSE06-D3(BJ)/LCAO(Cr17)	*
$PdTe_2$	CdI_2	4.006	4.006	5.106	90	90	120	1.15	PBE0/LCAO(Cr17)	*
$PdTe_2$	Pyrite	6.561	6.561	6.561	90	90	90	-	PBE0/LCAO(Cr17)	*

Table 6: Comparison of calculated and experimental lattice parameters for different methods from literature and this work (∗) for PdPS, PdP_2, and PtX_2. Cr17 refers to Crystal17, VASP to *Vienna Ab Initio Simulation Package*, and QE to *Quantum Espresso* PAW represents projector augmented waves, LCAO refers to linear combination of atomic orbitals, TMNCPP to Troullier-Martins type norm-conserving pseudopotentials. For details on the method please refer to the reference. MAD is the mean average deviation in %.

System	Structure	a	b	c	α	β	γ	MAD	Method	Ref.
PdPS	PdPS	13.607	5.674	5.687	90	90	90	2.238	PBE0/LCAO(Cr17)	∗
PdPSe	PdPS	13.900	5.831	5.866	90	90	90	2.403	PBE0/LCAO(Cr17)	∗
PdP_2	PdP_2	6.785	5.850	5.887	90	121.9	90	0.3	LDA+PW/PAW(VASP)	[38]
PdP_2	PdP_2	6.815	5.867	6.239	90	126.7	90	7.44	PBE0/LCAO(Cr17)	∗
PtS_2	CdI_2	3.570	3.570	6.320	90	90	120	25.45	PBE/PAW(VASP)	[42]
PtS_2	CdI_2	3.600	3.600	4.600	90	90	120	9.0	PBE+D3/PAW(VASP)	[42]
PtS_2	CdI_2	3.530	3.530	5.317	90	90	120	5.54	PBE0/LCAO(Cr17)	∗
$PtSe_2$	CdI_2	3.709	3.709	4.933	90	90	120	3.01	PBE0/LCAO(Cr17)	∗
$PtSe_2$	MoS_2	3.507	3.507	11.334	90	90	120	-	PBE0/LCAO(Cr17)	∗
$PtSe_2$	CdI_2	3.750	3.750	6.550	90	90	120	28.92	PBE/PAW(VASP)	[42]
$PtSe_2$	CdI_2	3.790	3.790	4.750	90	90	120	6.93	PBE+D3/PAW(VASP)	[42]
$PtTe_2$	CdI_2	4.031	4.031	5.275	90	90	120.0	1.04	PBE0/LCAO(Cr17)	∗
$PtTe_2$	MoS_2	3.879	3.879	11.957	90	90	120.0	-	PBE0/LCAO(Cr17)	∗

References

1. Oyedele, A. D. *et al.* $PdSe_2$: Pentagonal Two-Dimensional Layers with High Air Stability for Electronics. *Journal of the American Chemical Society* **139,** 14090–14097 (2017).
2. Sun, M. *et al.* Few-Layer $PdSe_2$ Sheets: Promising Thermoelectric Materials Driven by High Valley Convergence. *ACS Omega* **3,** 5971–5979 (2018).
3. Wang, Y., Li, Y. & Chen, Z. Not Your Familiar Two Dimensional Transition Metal Disulfide: Structural and Electronic Properties of the PdS_2 Monolayer. *Journal of Materials Chemistry C* **3,** 9603–9608 (2015).
4. Ghorbani-Asl, M. *et al.* A Single-Material Logical Junction Based on 2D Crystal PdS_2. *Advanced Materials* **28,** 853–856 (2016).
5. Lei, W. *et al.* Ferroelastic Lattice Rotation and Band-Gap Engineering in Quasi 2D Layered-Structure $PdSe_2$ under Uniaxial Stress. *Nanoscale* (2019).
6. Liu, G. *et al.* Negative Poisson's Ratio in Monolayer $PdSe_2$. *Computational Materials Science* **160,** 309–314 (2019).
7. Lei, W. *et al.* A New 2D High-Pressure Phase of $PdSe_2$ with High-Mobility Transport Anisotropy for Photovoltaic Applications. *Journal of Materials Chemistry C* **7,** 2096–2105 (2019).
8. Perdew, J. P., Ernzerhof, M. & Burke, K. Rationale for Mixing Exact Exchange with Density Functional Approximations. *J. Chem. Phys.* **105,** 9982 (1996).
9. Dovesi, R. *et al.* Quantum-Mechanical Condensed Matter Simulations with CRYSTAL. *Wiley Interdisciplinary Reviews: Computational Molecular Science* **8,** e1360 (2018).
10. Blum, V. *et al.* Ab Initio Molecular Simulations with Numeric Atom-Centered Orbitals. *Computer Physics Communications* **180,** 2175–2196 (2009).
11. Laun, J., Vilela Oliveira, D. & Bredow, T. Consistent Gaussian Basis Sets of Double- and Triple-Zeta Valence with Polarization Quality of the Fifth Period for Solid-State Calculations. eng. *Journal of Computational Chemistry* **39,** 1285–1290 (2018).
12. Kokalj, A. *et al.* Periodic DFT Study of the Pt(111): A p(1×1) Atomic Oxygen Interaction with the Surface. *The Journal of Physical Chemistry B* **103,** 7222–7232 (1999).
13. Perdew, J. P., Burke, K. & Ernzerhof, M. Generalized Gradient Approximation Made Simple. *Physical Review Letters* **77,** 3865–3868 (1996).
14. Grimme, S. Semiempirical GGA-type density functional constructed with a long-range dispersion correction. de. *Journal of Computational Chemistry* **27,** 1787–1799 (2006).
15. Grimme, S. *et al.* Dispersion-Corrected Mean-Field Electronic Structure Methods. *Chemical Reviews* **116,** 5105–5154 (2016).
16. Grimme, S. *et al.* A Consistent and Accurate Ab Initio Parametrization of Density Functional Dispersion Correction (DFT-D) for the 94 Elements H-Pu. *The Journal of Chemical Physics* **132,** 154104 (2010).
17. Becke, A. D. & Johnson, E. R. A Simple Effective Potential for Exchange. *The Journal of Chemical Physics* **124,** 221101 (2006).
18. Tkatchenko, A., Ambrosetti, A. & DiStasio, R. A. Interatomic Methods for the Dispersion Energy Derived from the Adiabatic Connection Fluctuation-Dissipation Theorem. *The Journal of Chemical Physics* **138,** 074106 (2013).
19. Tkatchenko, A. *et al.* Accurate and Efficient Method for Many-Body van Der Waals Interactions. *Physical Review Letters* **108,** 236402 (2012).
20. Heyd, J., Scuseria, G. E. & Ernzerhof, M. Hybrid Functionals Based on a Screened Coulomb Potential. *The Journal of Chemical Physics* **118,** 8207–8215 (2003).
21. Heyd, J. & Scuseria, G. E. Efficient Hybrid Density Functional Calculations in Solids: Assessment of the Heyd–Scuseria–Ernzerhof Screened Coulomb Hybrid Functional. *The Journal of Chemical Physics* **121,** 1187–1192 (2004).
22. Heyd, J., Scuseria, G. E. & Ernzerhof, M. Erratum: "Hybrid Functionals Based on a Screened Coulomb Potential" [J. Chem. Phys. 118, 8207 (2003)]. *The Journal of Chemical Physics* **124,** 219906 (2006).
23. Lacivita, V. *et al.* Static and Dynamic Coupled Perturbed Hartree-Fock Vibrational (Hyper)Polarizabilities of Polyacetylene Calculated by the Finite Field Nuclear Relaxation Method. *The Journal of Chemical Physics* **137,** 014103 (2012).

24. Ferrero, M. *et al.* Coupled Perturbed Hartree-Fock for Periodic Systems: The Role of Symmetry and Related Computational Aspects. *The Journal of Chemical Physics* **128,** 014110 (2008).
25. Ferrero, M. *et al.* The Calculation of Static Polarizabilities of 1-3D Periodic Compounds. the Implementation in the Crystal Code. *Journal of Computational Chemistry* **29,** 1450–1459 (2008).
26. Grønvold, F. & Røst, E. The Crystal Structure of $PdSe_2$ and PdS_2. *Acta Crystallographica* **10,** 329–331 (1957).
27. Hulliger, F. Electrical Properties of Some Nickel-Group Chalcogenides. *Journal of Physics and Chemistry of Solids* **26,** 639–645 (1965).
28. Selb, E. *et al.* Crystal Structures of the High-Pressure Palladium Dichalcogenides $Pd_{0.94(1)}S_2$ and $Pd_{0.88(1)}Se_2$ Comprising Exceptional Pd^{IV} Oxidation States. *Zeitschrift für anorganische und allgemeine Chemie* **643,** 1415–1423 (2017).
29. Zhang, G. *et al.* Optical and Electrical Properties of Two-Dimensional Palladium Diselenide. *Applied Physics Letters* **114,** 253102 (2019).
30. Larchev, V. N. & Popova, S. V. Polymorphism of Palladium Dichalcogenides at High Pressures and Temperatures. *Inorganic Materials* **14,** 611–612 (1978).
31. Selb, E., Tribus, M. & Heymann, G. Verbeekite, the Long-Unknown Crystal Structure of Monoclinic $PdSe_2$. *Inorganic Chemistry* **56,** 5885–5891 (2017).
32. Pell, M. A., Mironov, Y. V. & Ibers, J. A. $PdTe_2$. *Acta Crystallographica Section C: Crystal Structure Communications* **52,** 1331–1332 (1996).
33. Zachariasen, W. H. The Crystal Structure of Palladium Diphosphide. *Acta Crystallographica* **16,** 1253–1255 (1963).
34. Jeitschko, W. The Structure of PdPS and the Crystal Chemistry of Late Transition-Metal Dipnictides and Dichalcogenides. *Acta Crystallographica Section B: Structural Crystallography and Crystal Chemistry* **30,** 2565–2572 (1974).
35. Hulliger, F. *Structural Chemistry of Layer-Type Phases* (Springer Netherlands, 1976).
36. Grønvold, F. *et al.* On the Sulfides, Selenides, and Tellurides of Platinum. *Acta Chemica Scandinavica* **14,** 1879–1893 (1960).
37. Wang, Y. *et al.* Monolayer $PtSe_2$, a New Semiconducting Transition-Metal-Dichalcogenide, Epitaxially Grown by Direct Selenization of Pt. *Nano Letters* **15,** 4013–4018 (2015).
38. Hamidani, A., Bennecer, B. & Zanat, K. Structural and Electronic Properties of the Pseudo-Binary Compounds PdX_2 (X=P, S and Se). *Journal of Physics and Chemistry of Solids* **71,** 42–46 (2010).
39. Soulard, C. *et al.* Experimental and Theoretical Investigation on the Relative Stability of the PdS_2- and Pyrite-Type Structures of $PdSe_2$. *Inorganic Chemistry* **43,** 1943–1949 (2004).
40. Chow, W. L. *et al.* High Mobility 2D Palladium Diselenide Field-Effect Transistors with Tunable Ambipolar Characteristics. *Advanced Materials* **29,** 1602969 (2017).
41. Fei, F. *et al.* Nontrivial Berry Phase and Type-II Dirac Transport in the Layered Material $PdTe_2$. *Physical Review B* **96,** 041201 (2017).
42. Piotrowski, M. J., Nomiyama, R. K. & Da Silva, J. L. F. Role of van Der Waals Corrections for the PtX_2 (X=O,S,Se) Compounds. *Physical Review B* **88,** 075421 (2013).

Roman_Review_SI.pdf (9.56 MiB) view on ChemRxiv • download file